

# Effects of pore fluids on quasi-static shear modulus caused by pore-scale interfacial phenomena

Alexander Y. Rozhko\*

Department of Energy Resources, University of Stavanger, Kjell Arholmsgate 41, 4036 Stavanger, Norway

Received April 2019, revision accepted August 2019

## ABSTRACT

It is evident from the laboratory experiments that shear moduli of different porous isotropic rocks may show softening behaviour upon saturation. The shear softening means that the shear modulus of dry samples is higher than of saturated samples. Shear softening was observed both at low (seismic) frequencies and high (ultrasonic) frequencies. Shear softening is stronger at seismic frequencies than at ultrasonic frequencies, where the softening is compensated by hardening due to unrelaxed squirt flow. It contradicts to Gassmann's theory suggesting that the relaxed shear modulus of isotropic rock should not depend upon fluid saturation, provided that no chemical reaction between the solid frame and the pore fluid. Several researchers demonstrated that the shear softening effect is reversible during re-saturation of rock samples, suggesting no permanent chemical reaction between the solid frame and the pore fluid. Therefore, it is extremely difficult to explain this fluid–rock interaction mechanism theoretically, because it does not contradict to the assumptions of Gassmann's theory, but contradicts to its conclusions. We argue that the observed shear softening of partially saturated rocks by different pore fluids is related to pore-scale interfacial phenomena effects, typically neglected by the rock physics models. These interface phenomena effects are dependent on surface tension between immiscible fluids, rock wettability, aperture distribution of microcracks, compressibility of microcracks, porosity of microcracks, elastic properties of rock mineral, fluid saturation, effective stress and wave amplitude. Derived equations allow to estimate effects of pore fluids and saturation on the shear modulus and mechanical strength of rocks.

**Key words:** Shear softening, Interface phenomena, Partial saturation.

## INTRODUCTION

Understanding of fluid saturation effect on seismic and acoustic velocities are among key tasks for geoscientists. The Gassmann's theory is the most common way to explain how the seismic rock properties will be changed with the change of fluid saturation. According to Gassmann's theory, the relaxed shear modulus of isotropic porous rock should not depend on the fluid saturation, if there is no chemical reaction between the solid frame and the pore fluid (Gassmann 1951; Pride,

Berryman and Harris 2004; Mavko, Mukerji and Dvorkin 2009; Müller, Gurevich and Lebedev 2010). The Gassmann's theory is applicable in the low frequency (or quasi-static) limit, when there is enough time for the wave-induced pore pressures to equilibrate. If the frequency is high, there is not enough time for the wave-induced pore pressures to equilibrate. This would lead to increase of shear modulus due to the unrelaxed response at high frequencies (e.g. Mavko *et al.* 2009). Thus, according to available rock physics models, one should expect:

1. relaxed shear modulus of saturated rock is equal to shear modulus of dry rock  $\mu_{\text{sat}} = \mu_{\text{dry}}$  in the low frequency limit (Gassmann 1951);

\*E-mail: alexander.y.rozhko@uis.no

2. unrelaxed shear modulus of saturated rock is higher than shear modulus of dry rock  $\mu_{\text{sat}} > \mu_{\text{dry}}$  in the high frequency limit (e.g. Berryman 2005; Mavko *et al.* 2009).

There are several experimental studies which demonstrate a violation of our theoretical expectations due to so-called shear softening effect, when  $\mu_{\text{sat}} < \mu_{\text{dry}}$ , which was observed both at seismic and ultrasonic frequencies (e.g., Khazanehdari and Sothcott 2003; Adam, Batzle and Brevik 2006; Adam *et al.* 2009; Fabricius, Bächle and Eberli 2010; Adam and Otheim 2013; Bauer *et al.* 2016; Mikhaltsevitch, Lebedev and Gurevich 2016). Shear softening is stronger at seismic frequencies than at ultrasonic frequencies, where the softening is compensated by hardening due to unrelaxed squirt flow. Adam *et al.* (2006, 2009) reported shear modulus, measured on isotropic carbonate rocks at seismic and ultrasonic frequencies. Shear softening was observed for all samples at seismic frequencies and low confining pressure, whereas at high confining pressure shear softening is negligibly small for most of the samples. However, samples revealed either softening or stiffening at ultrasonic frequencies. Mikhaltsevitch *et al.* (2016) report both stiffening and softening of shear modulus both at seismic and ultrasonic frequencies for carbonate rocks. Furthermore, they demonstrated that stiffening or softening behaviour of shear modulus may depend on the pore fluid, which cannot be explained by Gassmann's theories. Vo-Thanh (1995) came to the same conclusion regarding the effect of pore fluid chemistry and saturation on acoustic velocities ultrasonic frequencies. Yin *et al.* (2019) report the shear softening of clay bearing sandstone at seismic and ultrasonic frequencies. Bauer *et al.* (2016) report experimental data at seismic and ultrasonic frequencies for sand, sandstone and shales suggesting that the Gassmann equations underestimate the observed velocity dispersion. Diethart-Jauk and Gegenhuber (2018) reported the shear softening behaviour at ultrasonic frequencies for different lithologies: limestone, dolomite, quartzite and basalt. Adam and Otheim (2013) reported shear softening effect observed at seismic frequencies on basalt rock and negligibly small stiffening effect at ultrasonic frequency. Lebedev, Wilson and Mikhaltsevitch (2014) reported softening of shear modulus of limestone sample observed at seismic frequencies.

Furthermore, several researchers reported the softening of elastic moduli observed during triaxial testing at large strains (e.g. Tutuncu, Podio and Sharma 1998; Risnes and Flaageng 1999; Baud, Zhu and Wong 2000; Risnes *et al.* 2003, 2005; David *et al.* 2015). Shear softening at ultrasonic frequencies for carbonate rocks were reported by Assefa, McCann and Sothcott (2003), Japsen *et al.* (2002), Røgen

*et al.* (2005) and Sharma *et al.* (2013). Both shear softening and shear stiffening at ultrasonic frequencies for carbonate rocks were reported by Baechle *et al.* (2005, 2009), Verwer, Braaksma and Kenter (2008), Fabricius *et al.* (2010), Vega, Prajapat and Al Mazrooei (2010), Verwer *et al.* (2010), Regnet *et al.* (2015) and Gegenhuber (2015), and for sandstone samples by Khazanehdari and Sothcott (2003), Bhuiyan and Holt (2016), Li *et al.* (2017, 2018).

To investigate if the reduction of frame modulus in carbonate rock is driven by chemical interaction, Baechle *et al.* (2005) conducted series of experiments in which saturation of carbonate samples were changed several times. They demonstrated that experimental results are reversible during re-saturation of rock samples. These results imply that there is no permanent frame moduli reduction due to chemical interaction of pore fluid with the rock frame. Risnes and Flaageng (1999), Risnes *et al.* (2003, 2005) obtained the same conclusion suggesting that the elastic moduli and strength are reversible during re-saturation of chalk with different pore liquids. These experiments suggest that dissolution and precipitation of calcite is not significant on the time scale when these experiments are conducted (Risnes and Flaageng 1999; Risnes *et al.* 2003, 2005; Baechle *et al.* 2005). Several researchers pointed out that the shear softening can be explained by chemical reaction of water with clay minerals (Yin *et al.* 2019). The chemical interaction of water with clay is well-documented in literature (e.g., Fjær *et al.* 2008); however, in our opinion it will lead to irreversible effect, and thus not relevant to explain the reversible effect of pore fluid, reported by Risnes and Flaageng (1999), Risnes *et al.* (2003, 2005) and Baechle *et al.* (2005). Murphy (1984) and Murphy, Winkler and Kleinberg (1986) conducted series of experiments to demonstrate that the water softening effect is taking place even in unconsolidated sandstones, which excludes water-softening mechanisms, such as swelling of clay cement, osmotic suction and dissolution and precipitation of calcite. The literature outlined above shows that physicochemical reasons for shear softening are not clear as it was stated in several publications (e.g. Japsen *et al.* 2002; Adam *et al.* 2006; Fabricius *et al.* 2010), especially when there is no evidence to chemical interaction of pore fluid with the rock frame.

In this paper, we demonstrate that the shear softening effect is related to the effect of hysteresis of liquid bridges in rocks containing partially saturated cracks. Here we are focusing on shear moduli of partially saturated rock, whereas bulk moduli were investigated by our previous publication (Rozhko 2019). The hysteresis of liquid bridges (described in the next section) is related to interface phenomena effects

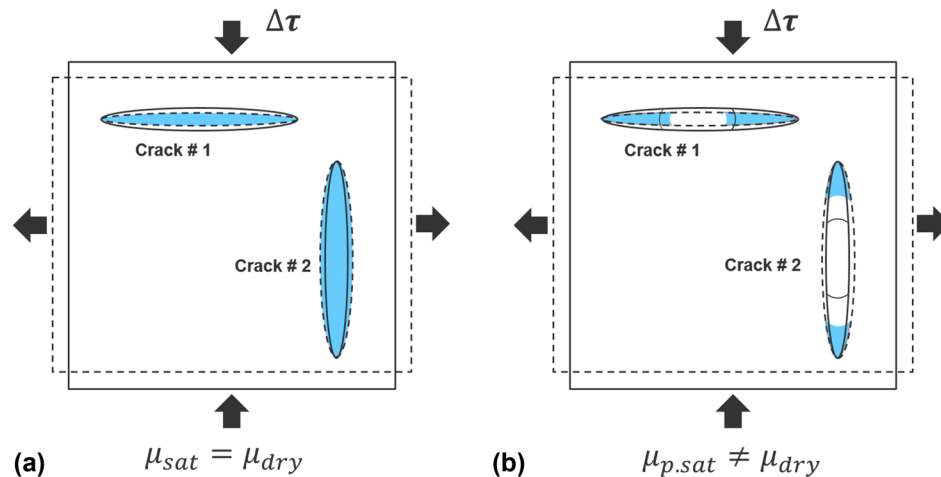


**Figure 1** Pure shear loading of isotropic (a) fully saturated rock and (b) partially saturated rock. Cracks # 1 and # 2 are identical and interconnected.

between immiscible fluid phases (such as water, gas or oil) and the solid inside compliant pores (cracks). The article is organized as follows. First, we introduce the hysteresis of liquid bridges effect in isotropic rock containing partially saturated cracks and argue that due to this effect the relaxed shear modulus is sensitive to the fluid saturation. Second, we derive mathematical equations to describe this effect numerically. Third, we introduce Betti–Rayleigh-reciprocity theorem (e.g., Schmeling 1985) for calculation of the effective shear modulus and attenuation of partially saturated rock. Then, we present numerical investigation of different input parameters of the model on the shear softening effect and shear attenuation. Next, we made the dimensional analysis of derived non-linear equations to demonstrate that the shear softening effect can be described by relatively simple equation. And finally, we discuss applications of the theory to reservoir rocks with log-normal distribution of micro-crack aperture.

### FLUID EFFECT ON RELAXED SHEAR MODULUS DUE TO HYSTERESIS OF LIQUID BRIDGES

Mavko *et al.* (2014, p. 138) suggested the following explanations for why Gassmann's relations only work at low frequencies and for isotropic rock. Imagine an isotropic sample of rock with cracks at all orientations. Under 'pure shear' loading, there is no volume change of the rock sample or the pore space, because some cracks open, whereas others close. According to Fig. 1(a), crack #1 decreases in volume, its pore pressure locally increases if the fluid cannot flow out of the crack, whereas crack #2 increases in volume, its pore pressure

locally decreases if the fluid cannot flow into the crack. If the frequency is too high, there is a tendency for local pore pressures to increase in some pores and decrease in others: hence, the shear modulus depends on the fluid bulk modulus. Greater bulk modulus of fluid makes it more difficult to deform undrained pores, thus the shear modulus increases with increase of fluid bulk modulus at high frequencies. However, if the frequency is low enough, the fluid has time to flow and adjust: there is no net pore volume change and thus no change of pore pressure, therefore the shear modulus is independent of the fluids. If the rock is anisotropic, under pure shear conditions, some cracks will be more open in one direction, whereas others less closed in perpendicular direction: hence, the shear modulus depends on the fluid bulk modulus.

Next, we apply the same approach as described above by Mavko *et al.* (2014) to demonstrate the opposite, that is why Gassmann's relations will not work at low frequencies for isotropic, but partially saturated rock (see Fig. 1b). The wetting phase (water) occupies narrow parts of the crack, whereas the non-wetting phase (gas or oil) occupies wide (central) parts of the crack. At the equilibrium condition, the fluid pressure in each fluid phase is different due to interface tension between immiscible fluids. It is not difficult to understand that the low frequency shear modulus of isotropic partially saturated rock would depend on the fluid saturation due to physical phenomenon: hysteresis of liquid bridges (e.g.: De Souza *et al.* 2008; Chen, Amirfazli and Tang 2013; Zhang 2016; Shi *et al.* 2018). Due to this phenomenon, the positive change of pore volume in one direction will not be compensated by a negative change of pore volume in the perpendicular direction and hence the shear modulus

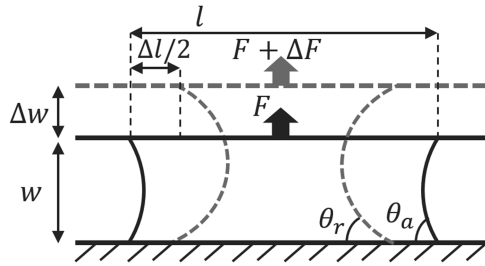


Figure 2 Deformation of the liquid bridge between two parallel plates.

will depend on the fluid content. Figure 2 shows a typical experimental setup used to investigate the hysteresis of liquid bridges between parallel plates (e.g. De Souza *et al.* 2008; Chen *et al.* 2013; Zhang 2016; Shi *et al.* 2018). The aperture between two plates is  $w$ , the diameter of wetted area is  $l$  and  $F$  is the force between two plates. A liquid drop is placed between two plates. The upper and the lower contact angles are  $\theta_a$  and  $\theta_r$  (i.e. advancing and receding angles). Here the

difference between advancing and receding contact angles is called a contact angle hysteresis. It depends on the contact line motion velocity. At zero velocity, a spectrum of static contact angles is observed (Bormashenko 2013a,b), which can be as large as tens of degrees (Ethington 1990). This effect is called a static contact angle hysteresis. The advancing contact angle increases with the contact line advancing velocity, whereas the receding contact angle decreases with the contact line receding velocity. This effect is called a dynamic contact angle hysteresis. In this paper, we address the Gassmann's theory which is a quasi-static theory. Thus, small dynamic corrections to the contact angle hysteresis during a quasi-static contact-line motion can be neglected. The change of aperture within a certain frequency  $\omega$  is  $\Delta w$ . Aperture changes induce changes of the force  $\Delta F$  and the diameter of wetted area  $\Delta l$ . Experiments are typically conducted under conditions when frequency  $\omega$  is low enough so that the viscous forces can be neglected. Figure 3 shows schematically typical experimental results

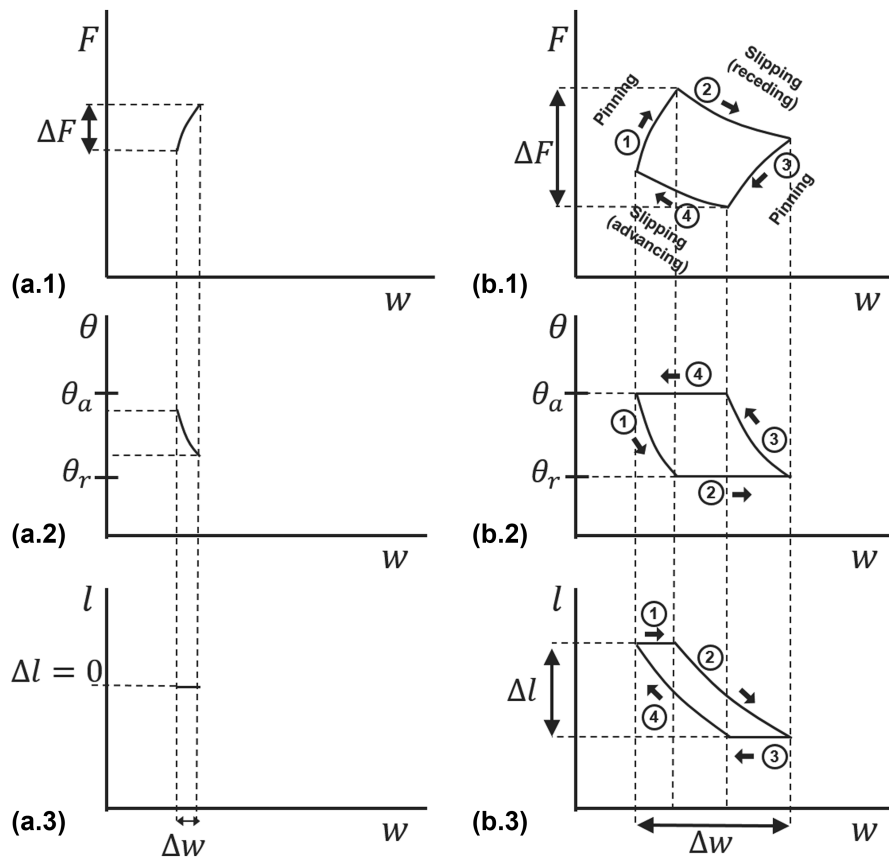


Figure 3 Effect of oscillation amplitude on hysteresis of liquid bridges (e.g. De Souza *et al.* 2008; Chen *et al.* 2013; Zhang 2016; Shi *et al.* 2018). If the oscillation amplitude is small, there is no hysteresis (a), whereas if the oscillation amplitude is large, there are four stages of hysteresis (b). (a1) and (b1) capillary force versus aperture (between two parallel plates); (a2) and (b2) contact angles versus aperture; (a3) and (b3) diameter of the wetted area (contact line displacement) versus aperture. Note here that Fig. 3(b) is corrected after Fig. 2(c) in Rozhko (2019).

showing the hysteresis of liquid bridges (e.g. De Souza *et al.* 2008; Chen *et al.* 2013; Zhang 2016; Shi *et al.* 2018). Figure 3(a1–a3) and (b1–b3) shows typical experimental results, obtained for different amplitudes of the aperture change  $\Delta w$ . Figure 3(a1,b1) shows capillary force versus aperture between parallel plates; Fig. 3(a2,b2) shows contact angles versus aperture; and Fig. 3(a3,b3) shows the diameter of the wetted area versus aperture. When the amplitude of the periodic aperture change is small, the contact line is pinned (*i.e.*  $\Delta l = 0$ , see Fig. 3a3) and the contact angle is changing within the range  $\theta_r < \theta_i + \Delta\theta < \theta_a$  (Fig. 3a2),  $\theta_i$  is the initial contact angle, which will be introduced later in this section. The change of the capillary force shows no hysteresis (Fig. 3a1), when the periodic amplitude of aperture change is small. The loading path (Fig. 3a1) coincides with unloading path. If the amplitude of the aperture change is increased, the amplitude of the contact angle change will increase as well. The amplitude of the contact angle change cannot exceed this range  $\theta_r \leq \theta_i + \Delta\theta \leq \theta_a$ , thus when the aperture change amplitude is sufficiently large, the contact angle will change between advancing and receding angles, as shown in Fig. 3(b2). At the time moment when the contact angle reaches advancing or receding angle, the contact line will slip (Fig. 3b3). Overall, the hysteresis of liquid bridges can be divided into four continuous stages, when the amplitude of the aperture change is sufficiently large, as shown in Fig. 3(b1–b3):

1. Pinning (stretching)
2. Slipping (receding)
3. Pinning (compression)
4. Slipping (advancing)

When the contact angle is greater than the receding angle, the aperture increase will result in an increase in the force due to pinning (Stage 1). This will be accompanied by a reduction in the contact angle until the receding angle is achieved when the force starts to decrease and the contact line starts to slip inward (Stage 2). If the aperture starts to decrease, the contact angle begins to increase until it reaches the advancing angle (Stage 3). In this stage, the pinning stage occurs again, which correspond to the reduction of capillary force. If the aperture keeps decreasing to the initial aperture, the contact line will slip outward with the contact angle equal to the advancing angle (Stage 4). The hysteresis of the capillary force leads to the energy dissipation due to the contact line friction mechanism. The contact line friction is the dominant mechanism of energy dissipation in these experiments. The intermolecular forces acting between molecules of the solid and those of the liquid, which pin the contact line to the

substrate, are responsible for the contact line friction, which occurs not over the entire solid–liquid interface, but only at the three-phase line (Yaminsky 2000; Bormashenko 2013a,b). Contact line friction occurs due to slippage and rolling of fluid molecules over the surface of the solid at the contact line location, *that is in one dimensional* (Ren and Weinan 2007). It is interesting to note here that viscous dissipation occurs in *three dimensional* due to interaction of fluid molecules moving with different velocities, whereas frictional dissipation between two solids in a contact occurs over a certain surface area in *two dimensional*. Thus, fundamentally, the contact line friction is different from other dissipation mechanisms.

Next, let us discuss the choice of initial contact angle ( $\theta_i$ ). In calculations, we assume that the initial contact angle is equal to the most stable Young's angle  $\theta_i = \theta_Y$ . It is important to note here that any contact angles within this range  $\theta_r < \theta < \theta_a$  are equilibrium contact angles; however, there is a most stable configuration of the equilibrium contact angle (e.g. Ruiz-Cabello, Rodríguez-Valverde and Cabrerizo-Vílchez 2014). The Young's contact angle is related to three coefficients of interfacial tension formed by the fluid–fluid interface with the solid surface (de Gennes, Brochard-Wyart and Quéré 2013). The equilibrium Young's contact angle can also be calculated from the advancing and receding contact angles, as was shown theoretically by Tadmor (2004) and confirmed experimentally by Chibowski (2008).

$$\cos(\theta_Y) = \frac{\Gamma_a \cos(\theta_a) + \Gamma_r \cos(\theta_r)}{\Gamma_a + \Gamma_r}, \quad (1)$$

$$\text{where } \Gamma_a = \frac{\sin(\theta_a)}{\sqrt[3]{2 - 3 \cos(\theta_a) + \cos^3(\theta_a)}} \text{ and}$$

$$\Gamma_r = \frac{\sin(\theta_r)}{\sqrt[3]{2 - 3 \cos(\theta_r) + \cos^3(\theta_r)}}.$$

Next, after introducing the hysteresis of liquid bridges phenomenon, we come back to the Fig. 1(b), showing two orthogonal partially saturated cracks under pure shear stress perturbation. It is clear without any mathematical calculations that due to hysteresis of the capillary forces (Fig. 3b1) the net change of pore volume in isotropic partially saturated rock will not be equal to 0. Hence, the shear modulus depends on the fluid saturation. The net change of the pore volume will be equal to 0 only if there is no hysteresis of capillary forces, *that is* when the contact line is pinned for small  $\Delta w$ . Hence, the net volume change of the partially saturated rock depends on the wave amplitude and will vanish in the limit when the wave amplitude is 0. It will be no dependence of shear modulus on the fluid if the surface

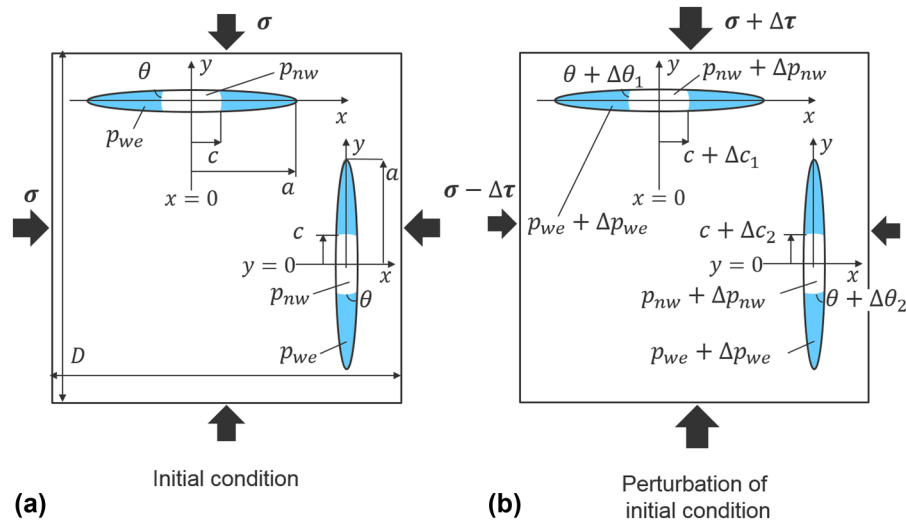


**Figure 4** (a) Initial equilibrium configuration of two identical (plane-strain) cracks:  $\sigma$  initial hydrostatic far-field compressive stress;  $p_{we}$  and  $p_{nw}$  initial pressure in the wetting and non-wetting fluid phases;  $\theta$  initial contact angle for the wetting phase;  $c$  initial contact line location. (b) Perturbation of the initial equilibrium configuration by the pure shear stress perturbation ( $\Delta\tau$ ). Perturbations of  $\Delta p_{we}$  and  $\Delta p_{nw}$  are identical in both (interconnected) cracks (in the low the frequency limit), whereas perturbations of contact angles  $\Delta\theta_i$  and contact line locations  $\Delta c_i$  are different in both cracks.

tension between immiscible fluid is 0, thus the change of the capillary force will be 0, that is  $\Delta F = 0$  for any  $\Delta w$ .

## MATHEMATICAL FORMULATION

In this section, we develop mathematical model, describing the hysteresis of liquid bridges in the rock containing two partially saturated cracks, shown in Fig. 4(a). The aim of this paper to demonstrate that the shear softening is caused by the hysteresis of liquid bridges in compliant cracks; that is why we are focusing only on the minimum number of input parameters required to describe this effect. Thus, we neglect porosity of channels which connect two cracks together, because otherwise we would also need to consider the distribution of pore throats and compressibilities of pore throats. Furthermore, real rocks contain cracks-like pores of different aspect ratio which are closed at different confining stress (e.g. Zimmerman 1990), while for simplicity we are considering only two identical cracks, which is sufficient for explanation of the shear softening effect by the hysteresis of liquid bridges without making the model too complex. Two identical plane-strain cracks (Crack #1 and Crack #2) are aligned along  $x$  and  $y$  directions, respectively. Initial geometries of two identical cracks are described by deformable elliptical cavities with semi-axes  $a$  and  $b$ . In calculations, we consider very narrow cracks with  $a \gg b$ . The distance between two cracks is sufficiently large, so that

the deformation and stress concentrations around one crack is not affected by deformation and stress concentrations around another crack (e.g. Zimmerman 1990). The deformation and stress concentration around cracks are affected only by fluid pressure inside cracks and stresses on the external boundary of the representative elementary volume (REV). The wetting fluid phase occupies thin parts of the crack (*i.e.* tips), whereas the non-wetting fluid phase occupies wide parts of the crack (centre). Pressures in the non-wetting ( $p_{nw}$ ) and wetting ( $p_{we}$ ) fluid phases are different due to interfacial tension and wettability effects and denoted here as capillary pressure ( $p_{cap}$ ) (e.g. Barenblatt, Entov and Ryzhik 1990):

$$p_{cap} = p_{nw} - p_{we}. \quad (2)$$

Initial saturation of two cracks is identical, as shown in Fig. 4(a). The fluid pressure acting on the surface of crack #1 is  $p_{nw}$  if  $|x| \leq c$  and  $p_{we}$  if  $c < |x| \leq a$ . Analogically, the fluid pressure acting on the surface of crack #2 is  $p_{nw}$  if  $|y| \leq c$  and  $p_{we}$  if  $c < |y| \leq a$  (Fig. 4a). The coordinate  $c$  defines the location of the contact line, as shown in Fig. 4(a). We consider a uniform initial far-field confining stress  $\sigma$ , acting on the external boundary of the REV, as shown in Fig. 4(a). Non-uniform initial far-field confining stress will result in different compressibilities along  $x$  and  $y$  directions, but we are not interested in this anisotropic case, because it contradicts to assumptions of Gassmann's theory, as it was discussed around

Fig. 1(a) in previous section. Cracks are assumed to be connected hydraulically, thus initial fluid pressure in each fluid phase is identical in two cracks. Furthermore, we consider a quasi-static deformation of the external boundary of REV, so that there is enough time for fluid pressure in each fluid phase to equilibrate between two cracks. The initial contact angle is equal to Young's angle  $\theta = \theta_Y$  in both cracks. Because the initial far-field normal stress, the initial fluid pressure and initial contact angles are identical in two identical cracks, the initial saturation degree is also identical in two cracks. Rozhko (2016), Rozhko and Bauer (2018) and Rozhko (2019) derived equations, describing the initial equilibrium saturation and the capillary pressure of partially saturated crack. The capillary pressure inside the equilibrium crack is calculated as follows (Rozhko 2016):

$$p_{\text{cap}} = \frac{\pi}{4} (p_{cl} + \sigma_n + p_{we}) \times \frac{1 - \sqrt{1 - 8p_{cl} \frac{\gamma \cos(\theta)}{\pi b} \frac{(\beta + \cot(\beta) \ln[\cos(\beta)] - \pi/2)}{(p_{cl} + \sigma_n + p_{we})^2 \sin(\beta)}}}{\beta + \cot(\beta) \ln[\cos(\beta)] - \pi/2}, \quad (3)$$

where  $p_{cl}$  is the crack closure pressure, calculated as (Rozhko 2016):

$$p_{cl} = \frac{b\mu}{a(1-\nu)}, \quad (4)$$

where  $\mu$  and  $\nu$  are the Shear modulus and Poisson's ratio of the rock mineral. The capillary pressure in equation (3) is two-way coupled to the deformation of the crack aperture. This equation follows from the Laplace equation and the analytical expression for the crack aperture at the contact line location (Rozhko 2016). In equation (3),  $\sigma_n$  is the far-field normal stress (i.e. normal to the crack surface), equal to  $\sigma$  at the initial condition, shown in Fig. 4(a). Here we are using a sign convention when compressive stresses, strains and displacements are negative, whereas compressive pressure is positive. In equation (3),  $\gamma$  is the surface tension between immiscible fluids and the angle  $\beta$  defines the location of the contact line:

$$\cos(\beta) = \frac{c}{a}. \quad (5)$$

The total volume of partially saturated crack ( $V_{\text{tot}}$ ) is calculated as (Rozhko 2016):

$$\frac{V_{\text{tot}}}{\pi ab} = 1 + \frac{\sigma_n + p_{we} + \left(1 + \frac{\sin(2\beta) - 2\beta}{\pi}\right) p_{\text{cap}}}{p_{cl}}. \quad (6)$$

Although the volume of the wetting fluid phase inside the partially saturated crack ( $V_{we}$ ) is calculated as (Rozhko and Bauer 2018; Rozhko 2019):

$$V_{we} = \tilde{V}_{we} + \delta V_{we} \quad (7)$$

where

$$\frac{\tilde{V}_{we}}{\pi ab} = \left(1 + \frac{\sigma_n + p_{we} + p_{\text{cap}} \left(1 + \frac{4}{\pi} \left[\frac{\beta \sin(2\beta) - \beta^2 + 2\cos^2(\beta) \ln[\cos(\beta)]}{2\beta - \sin(2\beta)}\right]\right)}{p_{cl}}\right) \times \frac{(2\beta - \sin(2\beta))}{\pi}. \quad (8)$$

And

$$\frac{\delta V_{we}}{b^2} = -\frac{(\pi - 2\theta - \sin(2\theta))}{\cos^2(\theta)} \sin^2(\beta) \times \left(1 + \frac{\sigma_n + p_{we} + \left(\frac{\pi - 2\beta - 2\cot(\beta) \ln[\cos(\beta)]}{\pi}\right) p_{\text{cap}}}{p_{cl}}\right)^2. \quad (9)$$

More details about derivation of above equations can be found in Rozhko (2016) and Rozhko and Bauer (2018).

The volume of the non-wetting phase inside the crack is calculated as

$$V_{nw} = V_{\text{tot}} - V_{we}. \quad (10)$$

The wetting-phase saturation of the crack ( $S_{we}$ ) is defined as

$$S_{we} = \frac{V_{we}}{V_{\text{tot}}} \quad (11)$$

Above equations are applicable for the following saturations range of the crack (see details in Rozhko and Bauer 2018):

$$\frac{b}{a} \leq S_{we} \leq 1 - \frac{b}{a}. \quad (12)$$

In calculations, we consider very narrow cracks,  $a \gg b$ , thus above equations are applicable almost for the entire range of saturations.

Next, following Mavko *et al.* (2014, p. 138), we consider the perturbations of the equilibrium state caused by a change in a far-field stress by 'pure shear' stress perturbation ( $\Delta\tau$ ) (Fig. 4.b). The amplitude of stress perturbation induced by seismic waves is very small (comparing to initial confining stress) typically around  $\Delta\tau \sim 10^2 - 10^4$  Pa. This pure shear stress perturbation induces perturbations of normal stresses:  $\Delta\sigma_{n,1} = \Delta\tau$  in the crack #1 and  $\Delta\sigma_{n,2} = -\Delta\tau$  in the crack #2. Here by sub-indexes  $i = 1$  or  $i = 2$ , we will denote

cracks #1 or crack #2, respectively. According to Fig. 4(b), the far-field ‘pure shear’ stress perturbation ( $\Delta\tau$ ) will also induce perturbations to the following parameters: (1) perturbation of the fluid pressure in the wetting phase  $\Delta p_{we}$ , (2) perturbation of the fluid pressure in the non-wetting phase  $\Delta p_{nw}$ , (3) perturbation of the contact line location  $\Delta c_i$  and (4) perturbation of the contact angle  $\Delta\theta_i$ . Here, we are considering the low frequency limit, when the fluid can flow between two cracks to equilibrate any gradients of fluid pressure in each fluid phase. Thus, the perturbation of fluid pressure in the wetting phase would be  $\Delta p_{we}$  and is identical in both cracks, as well as perturbation of the fluid pressure in the non-wetting phase would be  $\Delta p_{nw}$  and is identical in both cracks. Thus, perturbation of  $\Delta p_{cap} = \Delta p_{nw} - \Delta p_{we}$  is also identical in two cracks. Although perturbations of other parameters, shown in Fig. 4(b), are not identical, that is  $\Delta c_1 \neq \Delta c_2$ ,  $\Delta\theta_1 \neq \Delta\theta_2$  and  $\Delta\sigma_{n,1} \neq \Delta\sigma_{n,2}$ . Here, to be more specific, we can say that  $\Delta\sigma_{n,1} = -\Delta\sigma_{n,2}$  due to pure-shear perturbation of boundary conditions, whereas  $\Delta c_1 \neq -\Delta c_2$  and  $\Delta\theta_1 \neq -\Delta\theta_2$  due to non-linearity effects, as it will be discussed below.

To find perturbations of these parameters we need to consider perturbations of equilibrium parameters, such as perturbations of capillary pressure (in each crack), perturbations of crack volumes and perturbations of wetting phase volumes in both cracks. Because the hysteresis of liquid bridges is a highly non-linear effect, small stress perturbations of amplitude  $\Delta\tau \sim 10^2 - 10^4$  Pa are enough to cause this non-linearity due to deformation of highly compliant cracks. For example, recent publication of Rozhko and Bauer (2018) have shown that a small stress perturbation ( $\sim 10^2 - 10^4$  Pa) are sufficient to cause large changes in the contact angle  $\Delta\theta$  of the order of a few degrees or even larger. Thus, we cannot use linear (Taylor’s) expansions of equations (3), (6) and (7), because perturbations of  $\Delta\theta_i$  are large. However, we can consider a much smaller increment of the wave amplitude  $\Delta T$ :

$$\Delta T = \frac{\Delta\tau}{N_{\text{iter}}}, \quad (13)$$

where  $\Delta\tau$  is the wave induced pure shear stress perturbation, defined in Fig. 4(b), whereas  $N_{\text{iter}}$  is the number of iteration steps ( $N_{\text{iter}} \gg 1$ ). The number  $N_{\text{iter}}$  can be sufficiently large so that changes of all parameters, including  $\Delta\theta_i$  will be small. Typically,  $N_{\text{iter}} \sim 10a/b$  is sufficient to insure small deformations around crack aperture per stress increment  $\Delta T$ .

For sufficiently small stress increments, we can use linear (Taylor’s) expansions of equations (3), (6) and (7) for two cracks.

For crack # 1, Taylor’s expansion of equilibrium equations (3), (6) and (7) becomes

$$\Delta p_{\text{cap}} = \frac{\partial p_{\text{cap},1}}{\partial \sigma_{n,1}} \Delta T + \frac{\partial p_{\text{cap},1}}{\partial p_{we}} \Delta p_{we} + \frac{\partial p_{\text{cap},1}}{\partial \theta_1} \Delta \theta_1 + \frac{\partial p_{\text{cap},1}}{\partial \beta_1} \Delta \beta_1, \quad (14)$$

$$\Delta V_{\text{tot},1} = \frac{\partial V_{\text{tot},1}}{\partial \sigma_{n,1}} \Delta T + \frac{\partial V_{\text{tot},1}}{\partial p_{we}} \Delta p_{we} + \frac{\partial V_{\text{tot},1}}{\partial p_{\text{cap}}} \Delta p_{\text{cap}} + \frac{\partial V_{\text{tot},1}}{\partial \beta_1} \Delta \beta_1 \quad (15)$$

and

$$\Delta V_{we,1} = \frac{\partial V_{we,1}}{\partial \sigma_{n,1}} \Delta T + \frac{\partial V_{we,1}}{\partial p_{we}} \Delta p_{we} + \frac{\partial V_{we,1}}{\partial p_{\text{cap}}} \Delta p_{\text{cap}} + \frac{\partial V_{we,1}}{\partial \theta_1} \Delta \theta_1 + \frac{\partial V_{we,1}}{\partial \beta_1} \Delta \beta_1. \quad (16)$$

Similarly, for crack #2, Taylor’s expansion of equilibrium equations (3), (6) and (7) becomes

$$\Delta p_{\text{cap}} = -\frac{\partial p_{\text{cap},2}}{\partial \sigma_{n,2}} \Delta T + \frac{\partial p_{\text{cap},2}}{\partial p_{we}} \Delta p_{we} + \frac{\partial p_{\text{cap},2}}{\partial \theta_2} \Delta \theta_2 + \frac{\partial p_{\text{cap},2}}{\partial \beta_2} \Delta \beta_2, \quad (17)$$

$$\Delta V_{\text{tot},2} = -\frac{\partial V_{\text{tot},2}}{\partial \sigma_{n,2}} \Delta T + \frac{\partial V_{\text{tot},2}}{\partial p_{we}} \Delta p_{we} + \frac{\partial V_{\text{tot},2}}{\partial p_{\text{cap}}} \Delta p_{\text{cap}} + \frac{\partial V_{\text{tot},2}}{\partial \beta_2} \Delta \beta_2 \quad (18)$$

and

$$\Delta V_{we,2} = -\frac{\partial V_{we,2}}{\partial \sigma_{n,2}} \Delta T + \frac{\partial V_{we,2}}{\partial p_{we}} \Delta p_{we} + \frac{\partial V_{we,2}}{\partial p_{\text{cap}}} \Delta p_{\text{cap}} + \frac{\partial V_{we,2}}{\partial \theta_2} \Delta \theta_2 + \frac{\partial V_{we,2}}{\partial \beta_2} \Delta \beta_2. \quad (19)$$

In these equations, changes of normal stresses in two cracks are  $\Delta\sigma_{n,1} = \Delta T$  and  $\Delta\sigma_{n,2} = -\Delta T$ . All partial derivatives are calculated analytically and can be found in our previous publication Rozhko (2019).

Next, we are considering undrained boundary conditions, when there is no flow of the wetting and non-wetting



phases in or out of the external boundary of REV, while fluids can flow freely inside REV between two cracks. Thus, in our model, the masses of the wetting fluid and non-wetting fluid remain the same in the REV. In this case, changes of volumes of the wetting and non-wetting fluid phases are related to changes of pressures in those phases via the bulk moduli of the wetting ( $K_{we}$ ) and non-wetting ( $K_{nw}$ ) fluid phases as follows, where those changes are driven by small increment of the wave amplitude  $\Delta T$ :

$$(\Delta V_{we,1} + \Delta V_{we,2}) K_{we} = - (V_{we,1} + V_{we,2}) \Delta p_{we} \quad (20)$$

and

$$\begin{aligned} & (\Delta V_{tot,1} - \Delta V_{we,1} + \Delta V_{tot,2} - \Delta V_{we,2}) K_{nw} \\ &= - (V_{tot,1} - V_{we,1} + V_{tot,2} - V_{we,2}) \\ & \times (\Delta p_{we} + \Delta p_{cap}). \end{aligned} \quad (21)$$

It is interesting to note here that if we set  $K_{we} = 0$  and  $K_{nw} = 0$  in equations (20) and (21), we will get drained boundary conditions for REV, because perturbations of fluid pressure in each fluid phase will be equal to 0. Furthermore, one of the fluid phase can be under drained boundary conditions, whereas another fluid phase can be under undrained boundary condition. It can be modelled by setting corresponding fluid bulk modulus to 0 in equations (20) or (21). Thus, equations (20) and (21) embrace different types of boundary conditions for two immiscible fluids in REV: undrained, drained and mixed-mode boundary conditions.

Equations (14)–(21) are eight equations with 10 unknown parameters:  $\Delta p_{cap}$ ,  $\Delta p_{we}$ ,  $\Delta \theta_1$ ,  $\Delta \beta_1$ ,  $\Delta V_{tot,1}$ ,  $\Delta V_{we,1}$ ,  $\Delta \theta_2$ ,  $\Delta \beta_2$ ,  $\Delta V_{tot,2}$  and  $\Delta V_{we,2}$ . However, the number of unknown parameters will be reduced to eight, if we are considering either contact line pinning or the contact line motion conditions in two cracks. For example, the change of angle  $\Delta \beta_i$  in equations (14)–(19) is related to the change of the contact line location, according to equation (5). If the contact line is pinned, we have  $\Delta \beta_i = 0$  and  $\Delta \theta_i \neq 0$ ; whereas if the contact line moving, we have  $\Delta \beta_i \neq 0$  and  $\Delta \theta_i = 0$ . Thus, the system of equations (14)–(21) will have a unique solution if we are considering either the contact line pinning or the contact line motion conditions. In order to calculate response, produced by the stress perturbation  $\Delta \tau$ , we need to solve the system of equations (14)–(21)  $N_{iter}$  times (iterative solution). After each step, the following variable parameters need to be updated:

$$p_{we}^{(k)} = p_{we}^{(k-1)} + \Delta p_{we}, \quad (22)$$

$$\sigma_{n,1}^{(k)} = \sigma_{n,1}^{(k-1)} + \Delta T, \quad (23)$$

$$\beta_1^{(k)} = \beta_1^{(k-1)} + \Delta \beta_1, \quad (24)$$

$$\theta_1^{(k)} = \theta_1^{(k-1)} + \Delta \theta_1, \quad (25)$$

$$\sigma_{n,2}^{(k)} = \sigma_{n,2}^{(k-1)} - \Delta T, \quad (26)$$

$$\beta_2^{(k)} = \beta_2^{(k-1)} + \Delta \beta_2, \quad (27)$$

$$\theta_2^{(k)} = \theta_2^{(k-1)} + \Delta \theta_2. \quad (28)$$

In above equation, the super-script ( $k$ ) denotes the iteration step number, where  $k = 0$  denotes the initial conditions. We do not need to update other parameters, such as  $p_{cap}^{(k)}$ ,  $V_{tot,i}^{(k)}$  and  $V_{we,i}^{(k)}$ , because those parameters depend on  $p_{we}^{(k)}$ ,  $\sigma_{n,i}^{(k)}$ ,  $\beta_i^{(k)}$  and  $\theta_i^{(k)}$ , according to equations (3), (6) and (7), and thus can be calculated analytically. After applying equation (3) for both cracks, we will get  $p_{cap,1}^{(k)} = p_{cap,2}^{(k)}$ , as expected. After applying equations (6) and (7), we will get  $V_{tot,1}^{(k)} \neq V_{tot,2}^{(k)}$  and  $V_{we,1}^{(k)} \neq V_{we,2}^{(k)}$ . After each step, all partial derivatives which appear in equations (14)–(21) must be re-calculated as well, because they depend on  $p_{we}^{(k)}$ ,  $\sigma_{n,i}^{(k)}$ ,  $\beta_i^{(k)}$  and  $\theta_i^{(k)}$ . These parameters are identical for both cracks only at the initial conditions when ( $k = 0$ ). Furthermore, volumes of the wetting phase  $V_{we,i}$  and crack volumes  $V_{tot,i}$  should be updated after each step, in equations (20) and (21).

Next, we discuss more details about modelling the conditions when the contact line is pinned or moving. First, we define the contact line displacement, using equation (5) as follows:

$$\Delta c_i = -a \sin(\beta_i^{(k-1)}) \Delta \beta_i. \quad (29)$$

According to Fig. 4, the contact line moves to the receding direction if  $\Delta c_i > 0$  and to advancing direction if  $\Delta c_i < 0$ . Thus, the contact line in crack #  $i$  is pinned at the iteration step  $k$  if one of the following three conditions is taking place: (1) ( $\theta_r < \theta_i^{(k-1)} < \theta_a$ ); or when (2) ( $\theta_i^{(k-1)} = \theta_r$  and  $\Delta c_i < 0$ ); or when (3) ( $\theta_i^{(k-1)} = \theta_a$  and  $\Delta c_i > 0$ ). The contact line in crack #  $i$  at the iteration step  $k$  will be moving in advancing direction when ( $\theta_i^{(k-1)} = \theta_a$  and  $\Delta c_i < 0$ ) and will be moving in receding direction when ( $\theta_i^{(k-1)} = \theta_r$  and  $\Delta c_i > 0$ ). Next, we can derive analytical solutions to the system of linear equations (14)–(21) under four different conditions.

Case 1: The contact line is pinned in both cracks:

$$\begin{bmatrix} \Delta\theta_2 \\ \Delta p_{we} \\ \Delta p_{cap} \\ \Delta V_{we,1} \\ \Delta V_{tot,1} \\ \Delta\theta_1 \\ \Delta V_{we,2} \\ \Delta V_{tot,2} \end{bmatrix} = \Delta T \begin{bmatrix} 0 & V_{WE} & 0 & K_{we} & 0 & 0 & K_{we} & 0 \\ 0 & V_{NW} & V_{NW} & -K_{mw} & K_{mw} & 0 & -K_{mw} & K_{mw} \\ 0 & \frac{\partial p_{cap,1}}{\partial p_{we}} & -1 & 0 & 0 & \frac{\partial p_{cap,1}}{\partial \theta_1} & 0 & 0 \\ 0 & \frac{\partial V_{tot,1}}{\partial p_{we}} & \frac{\partial V_{tot,1}}{\partial p_{cap}} & 0 & -1 & 0 & 0 & 0 \\ 0 & \frac{\partial V_{we,1}}{\partial p_{we}} & \frac{\partial V_{we,1}}{\partial p_{cap}} & -1 & 0 & \frac{\partial V_{we,1}}{\partial \theta_1} & 0 & 0 \\ \frac{\partial p_{cap,2}}{\partial \theta_2} & \frac{\partial p_{cap,2}}{\partial p_{we}} & -1 & 0 & 0 & 0 & 0 & 0 \\ 0 & \frac{\partial V_{tot,2}}{\partial p_{we}} & \frac{\partial V_{tot,2}}{\partial p_{cap}} & 0 & 0 & 0 & 0 & -1 \\ \frac{\partial V_{we,2}}{\partial \theta_2} & \frac{\partial V_{we,2}}{\partial p_{we}} & \frac{\partial V_{we,2}}{\partial p_{cap}} & 0 & 0 & 0 & -1 & 0 \end{bmatrix}^{-1} \begin{pmatrix} 0 \\ 0 \\ -\frac{\partial p_{cap,1}}{\partial \sigma_{n,1}} \\ -\frac{\partial V_{tot,1}}{\partial \sigma_{n,1}} \\ -\frac{\partial V_{we,1}}{\partial \sigma_{n,1}} \\ \frac{\partial p_{cap,2}}{\partial \sigma_{n,2}} \\ \frac{\partial V_{tot,2}}{\partial \sigma_{n,2}} \\ \frac{\partial V_{we,2}}{\partial \sigma_{n,2}} \end{pmatrix} \quad (30)$$

Here for simplicity we defined volumes of the wetting phase inside two cracks as

$$V_{WE} = V_{we,1} + V_{we,2} \quad (31)$$

and volumes of the non-wetting phase as

$$V_{NW} = V_{tot,1} - V_{we,1} + V_{tot,2} - V_{we,2}. \quad (32)$$

Case 2: The contact line is moving in crack # 1, but pinned in crack # 2:

$$\begin{bmatrix} \Delta\theta_2 \\ \Delta p_{we} \\ \Delta p_{cap} \\ \Delta V_{we,1} \\ \Delta V_{tot,1} \\ \Delta\beta_1 \\ \Delta V_{we,2} \\ \Delta V_{tot,2} \end{bmatrix} = \Delta T \begin{bmatrix} 0 & V_{WE} & 0 & K_{we} & 0 & 0 & K_{we} & 0 \\ 0 & V_{NW} & V_{NW} & -K_{mw} & K_{mw} & 0 & -K_{mw} & K_{mw} \\ 0 & \frac{\partial p_{cap,1}}{\partial p_{we}} & -1 & 0 & 0 & \frac{\partial p_{cap,1}}{\partial \beta_1} & 0 & 0 \\ 0 & \frac{\partial V_{tot,1}}{\partial p_{we}} & \frac{\partial V_{tot,1}}{\partial p_{cap}} & 0 & -1 & \frac{\partial V_{tot,1}}{\partial \beta_1} & 0 & 0 \\ 0 & \frac{\partial V_{we,1}}{\partial p_{we}} & \frac{\partial V_{we,1}}{\partial p_{cap}} & -1 & 0 & \frac{\partial V_{we,1}}{\partial \beta_1} & 0 & 0 \\ \frac{\partial p_{cap,2}}{\partial \theta_2} & \frac{\partial p_{cap,2}}{\partial p_{we}} & -1 & 0 & 0 & 0 & 0 & 0 \\ 0 & \frac{\partial V_{tot,2}}{\partial p_{we}} & \frac{\partial V_{tot,2}}{\partial p_{cap}} & 0 & 0 & 0 & 0 & -1 \\ \frac{\partial V_{we,2}}{\partial \theta_2} & \frac{\partial V_{we,2}}{\partial p_{we}} & \frac{\partial V_{we,2}}{\partial p_{cap}} & 0 & 0 & 0 & -1 & 0 \end{bmatrix}^{-1} \begin{pmatrix} 0 \\ 0 \\ -\frac{\partial p_{cap,1}}{\partial \sigma_{n,1}} \\ -\frac{\partial V_{tot,1}}{\partial \sigma_{n,1}} \\ -\frac{\partial V_{we,1}}{\partial \sigma_{n,1}} \\ \frac{\partial p_{cap,2}}{\partial \sigma_{n,2}} \\ \frac{\partial V_{tot,2}}{\partial \sigma_{n,2}} \\ \frac{\partial V_{we,2}}{\partial \sigma_{n,2}} \end{pmatrix} \quad (33)$$

Case 3: The contact line is moving in crack # 2, but pinned in crack # 1:

$$\begin{bmatrix} \Delta\beta_2 \\ \Delta p_{we} \\ \Delta p_{cap} \\ \Delta V_{we,1} \\ \Delta V_{tot,1} \\ \Delta\theta_1 \\ \Delta V_{we,2} \\ \Delta V_{tot,2} \end{bmatrix} = \Delta T \begin{bmatrix} 0 & V_{WE} & 0 & K_{we} & 0 & 0 & K_{we} & 0 \\ 0 & V_{NW} & V_{NW} & -K_{nw} & K_{nw} & 0 & -K_{nw} & K_{nw} \\ 0 & \frac{\partial p_{cap,1}}{\partial p_{we}} & -1 & 0 & 0 & \frac{\partial p_{cap,1}}{\partial \theta_1} & 0 & 0 \\ 0 & \frac{\partial V_{tot,1}}{\partial p_{we}} & \frac{\partial V_{tot,1}}{\partial p_{cap}} & 0 & -1 & 0 & 0 & 0 \\ 0 & \frac{\partial V_{we,1}}{\partial p_{we}} & \frac{\partial V_{we,1}}{\partial p_{cap}} & -1 & 0 & \frac{\partial V_{we,1}}{\partial \theta_1} & 0 & 0 \\ \frac{\partial p_{cap,2}}{\partial \beta_2} & \frac{\partial p_{cap,2}}{\partial p_{we}} & -1 & 0 & 0 & 0 & 0 & 0 \\ \frac{\partial p_{cap,2}}{\partial \beta_2} & \frac{\partial V_{tot,2}}{\partial p_{we}} & \frac{\partial V_{tot,2}}{\partial p_{cap}} & 0 & 0 & 0 & 0 & -1 \\ \frac{\partial V_{we,2}}{\partial \beta_2} & \frac{\partial V_{we,2}}{\partial p_{we}} & \frac{\partial V_{we,2}}{\partial p_{cap}} & 0 & 0 & 0 & -1 & 0 \\ \frac{\partial V_{tot,2}}{\partial \beta_2} & \frac{\partial V_{tot,2}}{\partial p_{we}} & \frac{\partial V_{tot,2}}{\partial p_{cap}} & 0 & 0 & 0 & 0 & 0 \end{bmatrix}^{-1} \begin{pmatrix} 0 \\ 0 \\ -\frac{\partial p_{cap,1}}{\partial \sigma_{n,1}} \\ -\frac{\partial V_{tot,1}}{\partial \sigma_{n,1}} \\ -\frac{\partial V_{we,1}}{\partial \sigma_{n,1}} \\ \frac{\partial p_{cap,2}}{\partial \sigma_{n,2}} \\ \frac{\partial V_{tot,2}}{\partial \sigma_{n,2}} \\ \frac{\partial V_{we,2}}{\partial \sigma_{n,2}} \end{pmatrix} \quad (34)$$

Case 4, the contact line is moving in both cracks:

$$\begin{bmatrix} \Delta\beta_2 \\ \Delta p_{we} \\ \Delta p_{cap} \\ \Delta V_{we,1} \\ \Delta V_{tot,1} \\ \Delta\beta_1 \\ \Delta V_{we,2} \\ \Delta V_{tot,2} \end{bmatrix} = \Delta T \begin{bmatrix} 0 & V_{WE} & 0 & K_{we} & 0 & 0 & K_{we} & 0 \\ 0 & V_{NW} & V_{NW} & -K_{nw} & K_{nw} & 0 & -K_{nw} & K_{nw} \\ 0 & \frac{\partial p_{cap,1}}{\partial p_{we}} & -1 & 0 & 0 & \frac{\partial p_{cap,1}}{\partial \beta_1} & 0 & 0 \\ 0 & \frac{\partial V_{tot,1}}{\partial p_{we}} & \frac{\partial V_{tot,1}}{\partial p_{cap}} & 0 & -1 & \frac{\partial V_{tot,1}}{\partial \beta_1} & 0 & 0 \\ 0 & \frac{\partial V_{we,1}}{\partial p_{we}} & \frac{\partial V_{we,1}}{\partial p_{cap}} & -1 & 0 & \frac{\partial V_{we,1}}{\partial \beta_1} & 0 & 0 \\ \frac{\partial p_{cap,2}}{\partial \beta_2} & \frac{\partial p_{cap,2}}{\partial p_{we}} & -1 & 0 & 0 & 0 & 0 & 0 \\ \frac{\partial V_{tot,2}}{\partial \beta_2} & \frac{\partial V_{tot,2}}{\partial p_{we}} & \frac{\partial V_{tot,2}}{\partial p_{cap}} & 0 & 0 & 0 & 0 & -1 \\ \frac{\partial V_{we,2}}{\partial \beta_2} & \frac{\partial V_{we,2}}{\partial p_{we}} & \frac{\partial V_{we,2}}{\partial p_{cap}} & 0 & 0 & 0 & -1 & 0 \\ \frac{\partial V_{tot,2}}{\partial \beta_2} & \frac{\partial V_{tot,2}}{\partial p_{we}} & \frac{\partial V_{tot,2}}{\partial p_{cap}} & 0 & 0 & 0 & 0 & 0 \end{bmatrix}^{-1} \begin{pmatrix} 0 \\ 0 \\ -\frac{\partial p_{cap,1}}{\partial \sigma_{n,1}} \\ -\frac{\partial V_{tot,1}}{\partial \sigma_{n,1}} \\ -\frac{\partial V_{we,1}}{\partial \sigma_{n,1}} \\ \frac{\partial p_{cap,2}}{\partial \sigma_{n,2}} \\ \frac{\partial V_{tot,2}}{\partial \sigma_{n,2}} \\ \frac{\partial V_{we,2}}{\partial \sigma_{n,2}} \end{pmatrix} \quad (35)$$

Next, after solving the system of equations (14)–(21)  $N_{\text{iter}}$  times, we will find the response induced by the stress perturbation  $\Delta\tau$ , that is  $p_{we}^{(N_{\text{iter}})}$ ,  $\sigma_{n,i}^{(N_{\text{iter}})}$ ,  $\beta_i^{(N_{\text{iter}})}$  and  $\theta_i^{(N_{\text{iter}})}$ , where  $\sigma_{n,1}^{(N_{\text{iter}})} = \sigma_{n,1}^{(0)} + \Delta\tau$  and  $\sigma_{n,2}^{(N_{\text{iter}})} = \sigma_{n,2}^{(0)} - \Delta\tau$ . There is no explicit time dependence in this algorithm; however, the wave induced stress perturbation  $\Delta\tau$  can be a function of time. When we discretize  $\Delta\tau$  on much smaller stress increments, using equation (13) the time axis can also be discretized in the same manner accordingly. Thus, implicitly we can simulate any time-dependent signal using this algorithm by discretizing the wave-form on subintervals with subsequent numerical integration of equations of this paper.

### SHEAR MODULUS AND ATTENUATION IN PARTIALLY-SATURATED ROCK

In this section, a set of equations for the relaxed moduli and attenuation factors for a material containing two partially saturated cracks (Fig. 1b) will be given. Analytical solutions from the previous section describing wave-induced perturbations of fluid pressure and crack volumes will be utilized.

The effective elastic moduli of a material containing arbitrary inclusions can be obtained by using the Betti-Rayleigh-reciprocity theorem (Schmeling 1985; Mavko and Jizba 1991). It connects two elastic states of equilibrium of a linear elastic body. If these two states 1 and 2 are represented by the surface displacements  $\mathbf{u}_1$  and  $\mathbf{u}_2$  and the surface stress vectors or tractions  $\mathbf{T}_1$  and  $\mathbf{T}_2$  acting on the body, the theorem can be written as

$$\int_F \mathbf{T}_1 \cdot \mathbf{u}_2 dF = \int_F \mathbf{T}_2 \cdot \mathbf{u}_1 dF, \quad (36)$$

where the integration must be carried out over the total outer and inner surfaces  $F$  (e.g. Schmeling 1985). The shear modulus of the rock containing two partially saturated cracks (Fig. 1b) can be calculated by the following approach. Figure 5 shows two states of stresses and displacements, which can be connected using reciprocity theorem. Figure 5(a) shows the body containing cracks loaded by an external ‘pure shear’ tractions  $\Delta\tau$  and internal wave-induced perturbations of fluid pressure  $\Delta p_{fl,i}$  inside crack  $\#i$ . The change of fluid pressure in each crack depends on  $\Delta p_{we}$  and  $\Delta p_{cap}$ , which are identical in both cracks and also depends on the change of the contact line location  $\Delta c_i$ , which is different in both cracks, thus volume-average changes of fluid pressure are not identical in both cracks.  $\Delta p_{fl,i}$  is not uniform along the crack length, as it is shown in Fig. 5(a) by  $\Delta p_{fl,1}(x)$  and  $\Delta p_{fl,2}(y)$  for cracks  $\#1$  and  $\#2$ ,

respectively.  $\Delta U$  and  $\Delta \mathbf{u}$  shows body surface and pore wall displacements. In thin cracks, it is sufficient to consider only normal components of the crack wall displacements ( $\Delta \mathbf{u}_{y,1}(x)$  and  $\Delta \mathbf{u}_{x,2}(y)$ ), because tangential components are negligibly small. In Fig. 5(b), the body containing cracks is loaded by an external pure ‘shear tractions’  $\Delta\tau$ , the same as in Fig. 5(a). In Fig. 5(b), the thin cracks are loaded with tractions, the same as external tractions. Thus, the fluid pressure in crack  $\#1$  is  $\Delta p_{fl,1} = -\Delta\tau$  and inside crack  $\#2$  is  $\Delta p_{fl,2} = \Delta\tau$ . Here we remind for clarity that we are using a sign convention when compressive stresses are negative while compressive pressure is positive. The resulting displacements  $\Delta U_0$  and  $\Delta \mathbf{u}_0$  (Fig. 5b) are the same if cracks would contain solid matrix material (e.g. Schmeling 1985). Two states of stress in Fig. 5 can be combined by the reciprocity theorem giving:

$$\begin{aligned} \int_{F_{\text{ext}}} \Delta\tau \cdot \Delta U_0 dF_{\text{ext}} + \sum_{i=1}^2 \int_{F_{cr,i}} \Delta p_{fl,i}(x) \mathbf{n} \cdot \Delta \mathbf{u}_{0,i} dF_{cr} \\ = \int_{F_{\text{ext}}} \Delta\tau \cdot \Delta U dF_{\text{ext}} + \sum_{i=1}^2 \int_{F_{cr,i}} \Delta\tau \cdot \Delta \mathbf{u}_i dF_{cr}. \end{aligned} \quad (37)$$

Where, according to Figure 5, shear tractions are given by

$$\Delta\tau = - \begin{pmatrix} \Delta\tau & 0 & 0 \\ 0 & -\Delta\tau & 0 \\ 0 & 0 & 0 \end{pmatrix} \mathbf{n}, \quad (38)$$

$\mathbf{n}$  is the surface normal unit vector,  $F_{\text{ext}}$  is the total outer surface of representative elementary volume (REV) and  $F_{cr,i}$  is the surface of crack  $\#i$ . In equation (37), the summation is taken over two cracks.

The specific strain energy represented by the first integrals on either side of equation (37) can be taken to define the undisturbed shear modulus of rock mineral and effective shear modulus of REV, (e.g. Schmeling 1985):

$$\frac{1}{\mu_{\text{min}}} = \frac{1}{V_{\text{REV}} \Delta\tau^2} \int_{F_{\text{ext}}} \Delta\tau \cdot \Delta \mathbf{u}_0 dF_{\text{ext}} \quad (39)$$

and

$$\frac{1}{\mu_{\text{eff}}} = \frac{1}{V_{\text{REV}} \Delta\tau^2} \int_{F_{\text{ext}}} \Delta\tau \cdot \Delta U dF_{\text{ext}} \quad (40)$$

where  $V_{\text{REV}}$  is the volume of REV, which can be related to the initial crack porosity ( $n_c$ ) as follows:

$$V_{\text{REV}} = \frac{2\pi ab}{n_c}, \quad (41)$$

where the initial crack porosity is the porosity at zero effective stress.

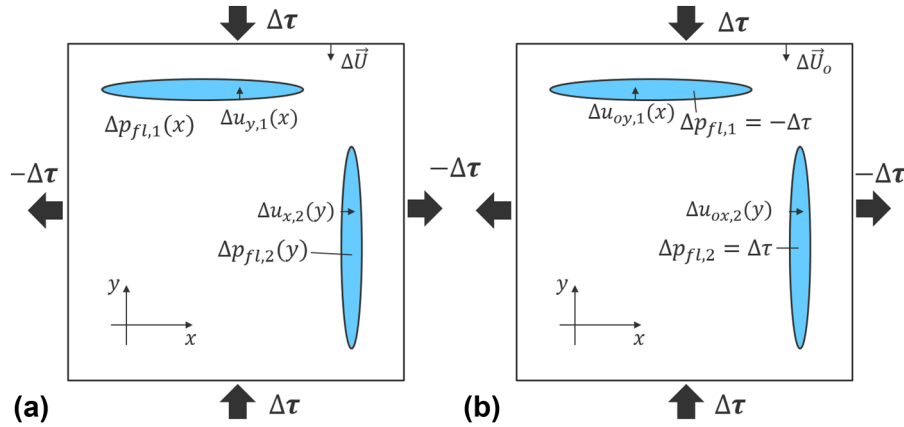


Figure 5 Illustration for the reciprocity theorem. For details, see text.

In equation (37), displacements of the crack wall  $\Delta \mathbf{u}_{0,i}$  are the same if the crack would contain the solid rock mineral, whereas displacements  $\Delta \mathbf{u}_i$  represent displacements of open crack that is partially saturated with water and gas. Because partially saturated crack is much more compressible than crack 'filled' with the solid rock mineral, we have  $|\Delta \mathbf{u}_i| \gg |\Delta \mathbf{u}_{0,i}|$ , hence the integration term  $\sum_{i=1}^2 \int_{F_{cr,i}} \Delta p_{fl,i}(\mathbf{x}) \mathbf{n} \cdot \Delta \mathbf{u}_{0,i} dF_{cr}$  in equation (37) can be neglected. Similar simplifications were also used in literature for more arbitrary pore geometries (e.g. Schmelung 1985).

In equation (40), the displacement on the outer boundary of REV (U) is unknown, however, using equations (37)–(41), we can still calculate the effective shear modulus of REV as follows:

$$\frac{1}{\mu_{\text{eff}}} = \frac{1}{\mu_{\text{min}}} - \frac{1}{V_{\text{REV}} \Delta \tau^2} \sum_{i=1}^2 \int_{F_{cr,i}} \Delta \tau \cdot \Delta \mathbf{u}_i dF_{cr} \quad (42)$$

In equation (42) the traction  $\Delta \tau$  is uniform inside the crack, thus the following simplification can be made:

$$\sum_{i=1}^2 \left( \int_{F_{cr,i}} \Delta \tau \cdot \Delta \mathbf{u}_i dF_{cr} \right) = \sum_{i=1}^2 \left( \Delta \tau \cdot \int_{F_{cr,i}} \Delta \mathbf{u}_i dF_{cr} \right), \quad (43)$$

where the integral  $\int_{F_{cr,i}} \Delta \mathbf{u}_i dF_{cr}$  represents the change in volume of crack #  $i$  due to deformation of crack aperture. The initial volume of crack #  $i$  is calculated using equation (6) and input parameters:  $p_{we,i}^{(k)}$ ,  $\sigma_{n,i}^{(k)}$ ,  $\beta_i^{(k)}$  and  $\theta_i^{(k)}$  at the iteration step  $k = 0$ , whereas the finale crack volume is calculated using input parameters in equation (6) at the iteration step  $k = N_{\text{iter}}$ . Note here that the capillary pressure, which appears in equation (6), is calculated using equation (3) and

the same input parameters:  $p_{we,i}^{(k)}$ ,  $\sigma_{n,i}^{(k)}$ ,  $\beta_i^{(k)}$  and  $\theta_i^{(k)}$ . Thus, we obtain:

$$\int_{F_{cr,i}} \Delta \mathbf{u}_i dF_{cr} = \Delta V_{\text{tot},i}, \quad (44)$$

where  $\Delta V_{\text{tot},i} = V_{\text{tot},i}^{(N_{\text{iter}})} - V_{\text{tot},i}^{(0)}$ . Because at initial conditions two cracks are identical, we have  $V_{\text{tot},1}^{(0)} = V_{\text{tot},2}^{(0)}$ , therefore  $\Delta V_{\text{tot},1}^{(N_{\text{iter}})} - \Delta V_{\text{tot},2}^{(N_{\text{iter}})} = V_{\text{tot},1}^{(N_{\text{iter}})} - V_{\text{tot},2}^{(N_{\text{iter}})}$ .

Hence,

$$\sum_{i=1}^2 \left( \int_{F_{cr,i}} \Delta \tau \cdot \Delta \mathbf{u}_i dF_{cr} \right) = -\Delta \tau \left( V_{\text{tot},1}^{(N_{\text{iter}})} - V_{\text{tot},2}^{(N_{\text{iter}})} \right) \quad (45)$$

Hence, equation (45) combined with equation (42) becomes:

$$\frac{1}{\mu_{\text{eff}}} = \frac{1}{\mu_{\text{min}}} + \frac{1}{\Delta \tau} \frac{V_{\text{tot},1}^{(N_{\text{iter}})} - V_{\text{tot},2}^{(N_{\text{iter}})}}{V_{\text{REV}}} \quad (46)$$

The above equation is very general and applicable for calculation of relaxed and unrelaxed shear modulus (in low and high frequency limits) of partially saturated, fully saturated and dry rocks. This equation depends on the change of crack volumes with applied stress perturbations, whereas the change of crack volumes depends on the fluid content of cracks. Furthermore, this equation can be applied to calculate effective shear modulus at any iteration step ( $k$ ), that is

$$\frac{1}{\mu_{\text{eff}}^{(k)}} = \frac{1}{\mu_{\text{min}}} + \frac{1}{\Delta \tau^{(k)}} \frac{V_{\text{tot},1}^{(k)} - V_{\text{tot},2}^{(k)}}{V_{\text{REV}}}, \quad (47)$$

where

$$\Delta \tau^{(k)} = \Delta \tau \frac{k}{N_{\text{iter}}}. \quad (48)$$

Thus, the shear strain of REV can be calculated at any iteration step  $k$  using equation:

$$\gamma_{\text{REV}}^{(k)} = \frac{\Delta\tau^{(k)}}{2\mu_{\text{eff}}^{(k)}} = \frac{\Delta\tau^{(k)}}{2\mu_{\text{min}}} + \frac{V_{\text{tot},1}^{(k)} - V_{\text{tot},2}^{(k)}}{2V_{\text{REV}}}. \quad (49)$$

Using equation (49), we can calculate the elastic strain energy of REV, induced by stress perturbation  $\Delta\tau$  as follows:

$$W = \frac{1}{2} \Delta\tau \gamma_{\text{REV}}^{(N_{\text{iter}})}. \quad (50)$$

Note here that equation (50) does not represent the absolute elastic energy, but only the wave energy, caused by transient stress  $\Delta\tau$ .

The attenuation of elastic wave energy can be calculated by the integration of the elastic energy over period of the elastic wave, that is

$$\delta W = \oint_{\text{Period}} \gamma_{\text{REV}}^{(k)} d\Delta\tau. \quad (51)$$

Equation (51) suggests that elastic wave energy will be attenuated if there is a hysteresis of shear strain during loading and unloading cycles. The attenuation factor  $\frac{1}{Q}$  is defined as a fraction of energy dissipated over wave period (Mavko *et al.* 2009; Müller *et al.* 2010).

$$\frac{1}{Q} = \frac{1}{2\pi} \frac{\delta W}{W}. \quad (52)$$

Next, it will be interesting to compare results, derived for partially saturated rock with results, calculated for dry rock or for fully saturated rock with a single fluid phase. If we are considering a dry rock with two cracks or fully saturated rock (single phase) in the low frequency limit (relaxed modulus), equation (46) yields

$$\frac{1}{\mu_{\text{dry}}} = \frac{1}{\mu_{\text{min}}} + \frac{n_c}{p_{cl}}. \quad (53)$$

Equation (53) directly follows from equation (6) in which  $p_{we} = p_{fl} = \text{const}$  and  $p_{\text{cap}} = 0$  due to full saturation of cracks. Equation (53) does not depend explicitly on the effective stress  $\sigma' = \sigma + p_{fl}$  (negative in compression); however, this equation is applicable as long as cracks are open, when  $p_{cl} + \sigma + p_{fl} > 0$ . If cracks are closed, the rock will deform as if there are no cracks, thus effective rock moduli will be equal to moduli of the rock mineral, that is  $\mu_{\text{dry}} = \mu_{\text{min}}$ . If the rock contains many cracks of different aspect ratio, those cracks will be closed at different effective confining stress (e.g. Zimmerman 1990). Thus, apparent shear modulus of dry rocks containing cracks of different aspect ratio will depend on the effective confining stress (e.g. Zimmerman 1990). In

this paper, we are considering only two identical cracks for simplicity. However, the model can be extended to more realistic case of many cracks with different length and aspect ratio. This, more realistic case will be considered at the end of this paper. Furthermore, equation (53) does not depend on the fluid compressibility, because in the low frequency limit the change of fluid pressure (induced by pure shear stress perturbation) will be 0 in isotropic rock. Thus, in equation (53), we re-derived conclusion obtained by Gassmann's that  $\mu_{\text{sat}} = \mu_{\text{dry}}$ , which is valid for isotropic rock at low frequency when the pore fluid does not interact with the rock frame.

## NUMERICAL RESULTS AND DIMENSIONAL ANALYSIS

In this section, we present numerical results for shear moduli ( $\mu_{\text{eff}}$ ) and seismic attenuation ( $\frac{1}{Q}$ ), calculated for representative elementary volume with two partially saturated cracks. In calculations, we will apply a periodic 'pure-shear' stress perturbation to the external boundary of representative elementary volume (REV), as shown in Fig. 6(a). The first cycle is shown by continuous black curve, whereas subsequent cycles are shown by the red dashed curve in Fig. 6(a). Figure 6(b) shows calculated stress-strain hysteresis of REV with two cracks, partially saturated with water and gas system with 50% of water saturation ( $S_{we} = 0.5$ ). Other input parameters of the model are given in Table 1. This saturation degree (and input parameters from Table 1) corresponds to initial capillary pressure of  $p_{\text{cap}} = 0.56$  MPa, calculated using equations (3) and (11). Similar to Fig. 6(a), the first cycle of the stress-strain hysteresis is shown by continuous black curve in Fig. 6(b), whereas subsequent cycles are shown by the red dashed curve. Calculations show that subsequent cycles do not return to its initial value with  $\gamma_{\text{REV}} = 0$  and  $\Delta\tau = 0$ . According to equation (49), the effective shear modulus of REV is inversely proportional to the slope of largest diagonal of the tetragon, shown in Fig. 6(a), whereas the attenuated energy is proportional to the area of the tetragon, according to equation (51). Figure 7 shows calculated changes of other parameters of the model. Alteration of fluid pressure in the wetting and non-wetting phases are shown in Fig. 7(a,b), respectively. Calculations show that amplitudes of the wave-induced fluid pressure perturbations are negligibly small, comparing to the wave amplitude. Similar to Fig. 6, the first cycle is shown by continuous black curve, whereas subsequent cycles are shown by the red dashed curve in Fig. 7. Figure 7(c,d) shows alterations of the contact line location in the first and second cracks, whereas Fig. 7(e,f)

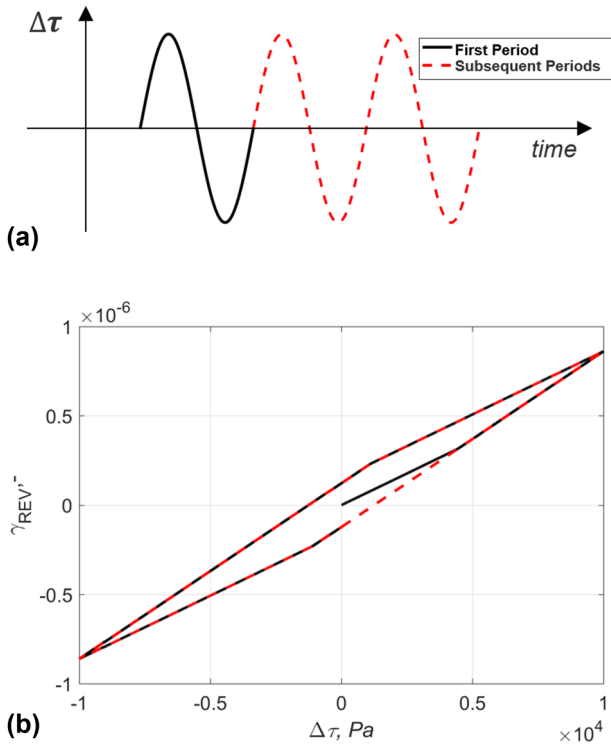


**Figure 6** (a) Applied a periodic ‘pure-shear’ stress perturbation to the external boundary of REV. (b) Calculated stress–strain hysteresis of REV with two cracks, partially saturated with water and gas system with 50% water saturation ( $S_{we} = 0.5$ ). Other input parameters of the model are given in Table 1. In (a) and (b), the first cycle is shown by continuous black curve, whereas subsequent cycles are shown by the red dashed curve. See Fig. 7 for changes of other parameters of the model.

shows alterations of the contact angles in the first and second cracks. Overall calculations of Figs 6 and 7 show that the hysteresis of liquid bridges is highly non-linear process, leading to the attenuation of the wave energy in the low (static) frequency limit. This non-linearity is highly sensitive to the wave amplitude, as it was discussed around Fig. 3. Next, we will investigate how the wave amplitude affect this non-linearity and how this will affect the effective shear modulus and attenuation in partially saturated rocks. We will consider both gas–water and oil–water systems. Assumed input parameters for both systems are given in Table 1, showing that the surface tension between gas and water interface is about 2.5 times higher than the surface tension for oil and water interface. Also, the gas phase is less wetting phase comparing to oil phase, as it is reflected in assumed input contact angles for the water phase. Also, the assumed bulk modulus of oil is much greater than the bulk modulus of gas, as shown in

**Table 1** Input parameters

Parameter	Value
Shear modulus of mineral ( $\mu_{min}$ )	12 GPa
Poisson’s ratio ( $\nu_{min}$ )	0.3
Water (brine) bulk modulus ( $K_{we}$ )	2.6 GPa
Gas bulk modulus ( $K_{mw}$ )	0.002 GPa
Oil bulk modulus ( $K_{mo}$ )	1.2 GPa
Surface tension between water and gas ( $\gamma$ )	0.073 Pa $\times$ m
Surface tension between water and oil ( $\gamma$ )	0.029 Pa $\times$ m
Advancing contact angle for wetting phase in water–gas system ( $\theta_a$ )	5°
Receding contact angle for wetting phase in water–gas system ( $\theta_r$ )	1°
Advancing contact angle for wetting phase in water–oil system ( $\theta_a$ )	37°
Receding contact angle for wetting phase in water–oil system ( $\theta_r$ )	35°
Initial crack porosity ( $n_c$ )	10 <sup>-3</sup>
Major semi-axis ( $a$ )	10 <sup>-3</sup> m
Initial aspect ratio ( $b/a$ )	10 <sup>-4</sup>
Effective stress ( $\sigma + p_{we}$ )	–15 MPa

Table 1. Figure 8(a) shows calculated effective shear modulus as a function of the wave-amplitude calculated for partially saturated rock with gas–water and oil–water systems, at water saturations  $S_{we} = 0.3$  and  $S_{we} = 0.6$ . Dashed black curve in Fig. 8(a) shows the shear modulus of dry rock. Calculations show that the shear softening effect depends on the wave amplitude and on the type of fluid and saturation degree. When the wave amplitude is small, the shear modulus of partially saturated rock coincides with shear modulus of dry rock. At small wave amplitude, the contact line is pinned, whereas if the contact line is slipping, the shear modulus of partially saturated rock is decreased. Wang, Schmitt and Wang (2015) argued that, due to the slippage at the solid–fluid interface, the stiffness of the rock will be lower than predicted by Biot–Gassmann models, which assume Stoke’s no-slip boundary conditions between fluid and solid. Our theoretical calculations support Wang *et al.* (2015) explanation, because the Stoke’s no-slip boundary conditions are not applicable at the contact line location (Ren and Weinan 2007). The contact line motion occurs by slippage and rolling of fluid molecules over the surface of the solid at the contact line location (Ren and Weinan 2007), this leads to the shear softening, predicted only when the contact line is moving. Calculations of Fig. 8(a) show that the shear softening occurs at certain critical wave amplitude  $\Delta\tau_c$ . At this wave amplitude, the contact line starts to move causing both shear softening and attenuation of elastic wave energy by the contact line friction mechanism.

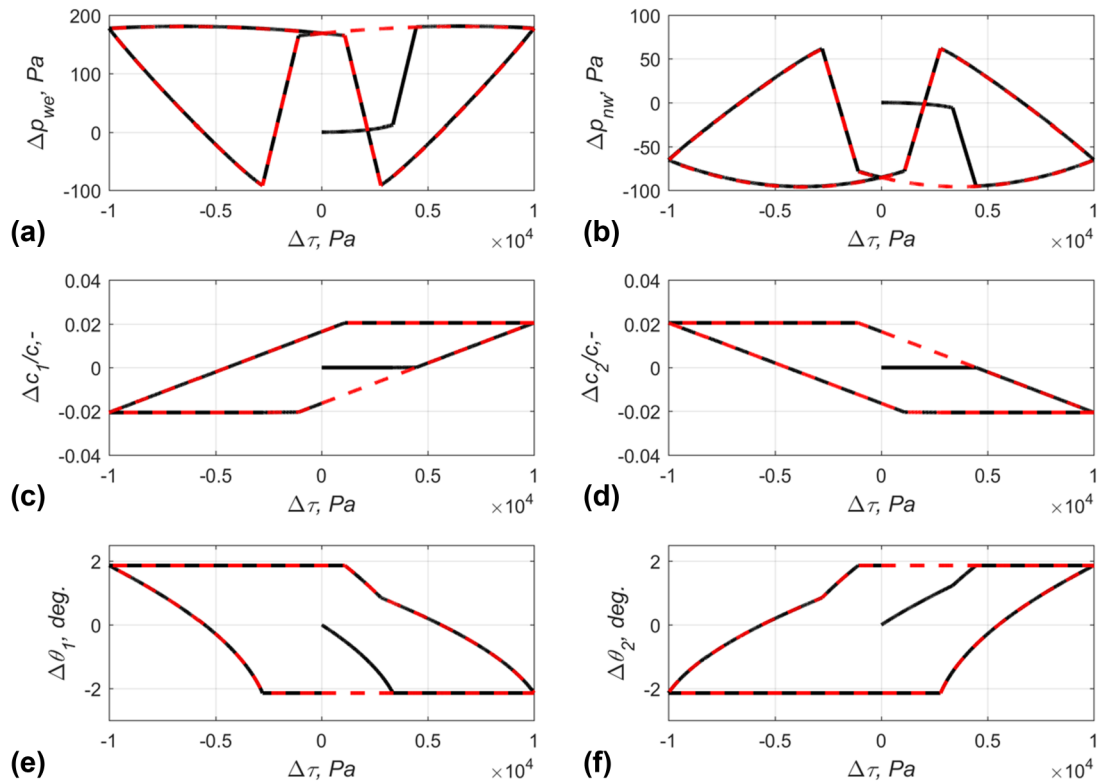


**Figure 7** (a) and (b) show calculated changes of fluid pressure in the wetting and non-wetting fluid phases, respectively; (c) and (d) show calculated changes of the contact line location in the first and second cracks, respectively; (e) and (f) show calculated changes of the contact angles in the first and second cracks. See also captions to Fig. 6.

Figure 8(a) shows that the shear softening is stronger for gas–water system as compared to oil–water system. Furthermore, Fig. 8(a) shows that the shear softening occurs at lower wave amplitude for gas–water system as compared to oil–water system. Figure 8(b) shows calculated attenuation factors for corresponding cases shown in Fig. 8(a). Calculations show that the attenuation is higher for gas–water system as compared to oil–water system.

Next, we will perform the dimensional analysis to understand better the impact of different input parameters on the shear softening and on the wave attenuation in partially saturated rocks. The shear softening is highly non-linear process described by the system of coupled equations, which are solved iteratively. However, to understand the physics, we will neglect the non-linearity and iterations. First, we will estimate the critical stress perturbation required for the onset of the contact line motion  $\Delta\tau_c$ . To do so, we will use the system of linear equations (30) in which all coefficients are calculated at the initial conditions, that is at zero interaction step ( $k = 0$ ), whereas the change of the contact angle, required for the onset of the contact line motion, is selected

(approximately) as  $|\Delta\theta_1| = \frac{\theta_a - \theta_r}{2}$  and  $\Delta\theta_1 = -\Delta\theta_2$ . The initial contact angle is equal to Young's angle and calculated with equations (1), which predicts approximately intermediate angle between advancing and receding angles, that is  $\theta_Y \approx \frac{\theta_a + \theta_r}{2}$ . Thus, the change of initial angle by  $\Delta\theta_1$  or by  $\Delta\theta_2$  will initiate the contact line slippage. Because we neglect the non-linearity and iterations, the system of equations (30) yields the following simplified equations, for the critical wave amplitude, required for the onset of the contact line motion:

$$\Delta\tau_c = \frac{(\theta_r - \theta_a) \frac{\partial p_{\text{cap}}}{\partial \theta}}{2 \frac{\partial p_{\text{cap}}}{\partial \sigma}}. \quad (54)$$

Partial derivatives in this equation are calculated at initial conditions using equations (A37) and (A39) from Rozhko (2019).

Next, we will estimate the amplitude of shear softening using the system of equations (35) when the contact line is moving in two cracks. In this case, we will assume sufficiently large wave amplitudes ( $\gg \Delta\tau_c$ ) when the contact line motion is much larger than the amplitude of the meniscus bending.



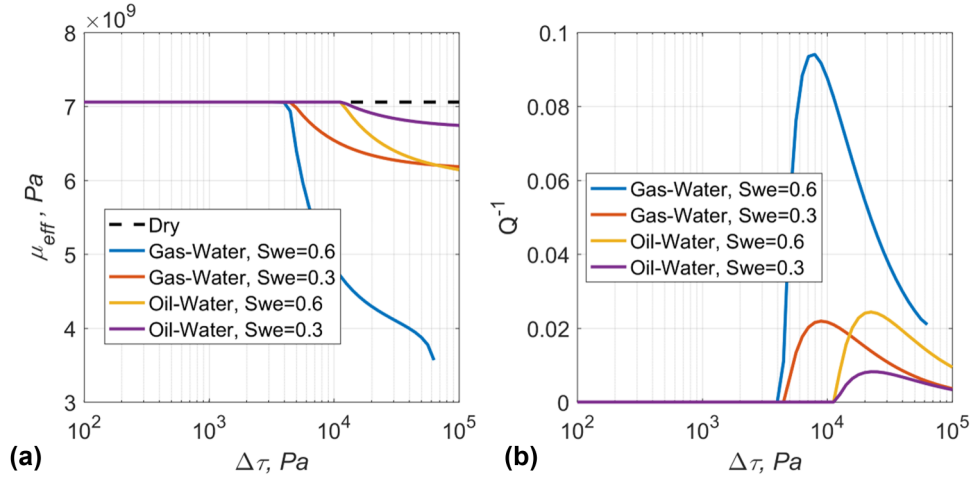


**Figure 8** (a) and (b) show calculated effective shear modulus and attenuation factor as a function of the wave-amplitude for the rock that is partially saturated with gas–water and oil–water systems, at water saturations of  $S_{we} = 0.3$  and  $S_{we} = 0.6$ . Dashed black curve in (a) shows the shear modulus of dry rock. Other input parameters of the model are given in Table 1.

After neglecting the non-linear effects in the system of equations (35), we can derive the expression for the difference between  $\Delta V_{\text{tot},1}$  and  $\Delta V_{\text{tot},2}$ , which will be used in equation (46) to derive the effective shear modulus of partially saturated rock. After all simplifications using equations (35), (41), (46), (53) and equations (A40) and (A41) from Rozhko (2019), the following expression for the effective shear modulus of partially saturated rock is derived:

$$\frac{1}{\mu_{p,\text{sat}}} = \frac{1}{\mu_{\text{dry}}} + \left( \frac{1}{\mu_{\text{dry}}} - \frac{1}{\mu_{\text{min}}} \right) \times \frac{2}{\pi} (1 - \cos(2\beta)) p_{\text{cap}} \left( \frac{\partial p_{\text{cap}}}{\partial \sigma} / \frac{\partial p_{\text{cap}}}{\partial \beta} \right). \quad (55)$$

All partial derivatives in equation (55) ( $\frac{\partial p_{\text{cap}}}{\partial \sigma}$  and  $\frac{\partial p_{\text{cap}}}{\partial \beta}$ ) are calculated analytically in Rozhko (2019) (equations A37 and A36). The first partial derivative  $\frac{\partial p_{\text{cap}}}{\partial \sigma}$  has a quite clear physical interpretation showing how the capillary pressure in the crack is changing with the change of the effective confining stress when all other parameters are kept constant. The second partial derivative ( $\frac{\partial p_{\text{cap}}}{\partial \beta}$ ) has less transparent physical meaning, because the angle  $\beta$  is related somehow to the contact line location inside the crack, according to equation (5). Let us understand better the physical interpretation of equation (55). To do so, let us first consider the equation (6). From this equation, we can see that the total volume of partially saturated crack is controlled by the following effective stress (e.g. Santos *et al.* 1990):

$$\sigma'_n = \sigma_n + p_{nw} - \chi p_{\text{cap}}. \quad (56)$$

This effective stress is sometimes referred in literature to as the generalized effective stress or the Bishop's effective stress (e.g. Fjær *et al.* 2008).

The effective stress coefficient, which appears in equation (56) is calculated using equation (5) as follows:

$$\chi = \frac{2\beta - \sin(2\beta)}{\pi}. \quad (57)$$

Next, using the differentiation rule  $\frac{\partial p_{\text{cap}}}{\partial \beta} = \frac{\partial p_{\text{cap}}}{\partial \chi} \cdot \frac{\partial \chi}{\partial \beta}$  we can substitute  $\frac{\partial p_{\text{cap}}}{\partial \beta} = \frac{2}{\pi}(1 - \cos(2\beta)) \frac{\partial p_{\text{cap}}}{\partial \chi}$  into equation (55) to derive the following expression for the effective shear modulus of partially saturated rock:

$$\frac{1}{\mu_{p,\text{sat}}} = \frac{1}{\mu_{\text{dry}}} + \left( \frac{1}{\mu_{\text{dry}}} - \frac{1}{\mu_{\text{min}}} \right) p_{\text{cap}} \left( \frac{\partial p_{\text{cap}}}{\partial \sigma} / \frac{\partial p_{\text{cap}}}{\partial \chi} \right). \quad (58)$$

This equation (58) is more understandable than equation (55) from the physical point of view; however, it is still difficult to see how the capillary pressure is changing with the effective stress coefficient while all other parameters are kept constant. In the recent publication of Rozhko (2016), it was demonstrated that the effective stress coefficient, controlling the volume of partially-saturated crack can be well approximated by the wetting-phase saturation:

$$\chi \approx S_{we}. \quad (59)$$

Thus, the equation (58) can be simplified further as

$$\frac{1}{\mu_{p,\text{sat}}} \approx \frac{1}{\mu_{\text{dry}}} + \left( \frac{1}{\mu_{\text{dry}}} - \frac{1}{\mu_{\text{min}}} \right) p_{\text{cap}} \left( \frac{\partial p_{\text{cap}}}{\partial \sigma} / \frac{\partial p_{\text{cap}}}{\partial S_{we}} \right). \quad (60)$$

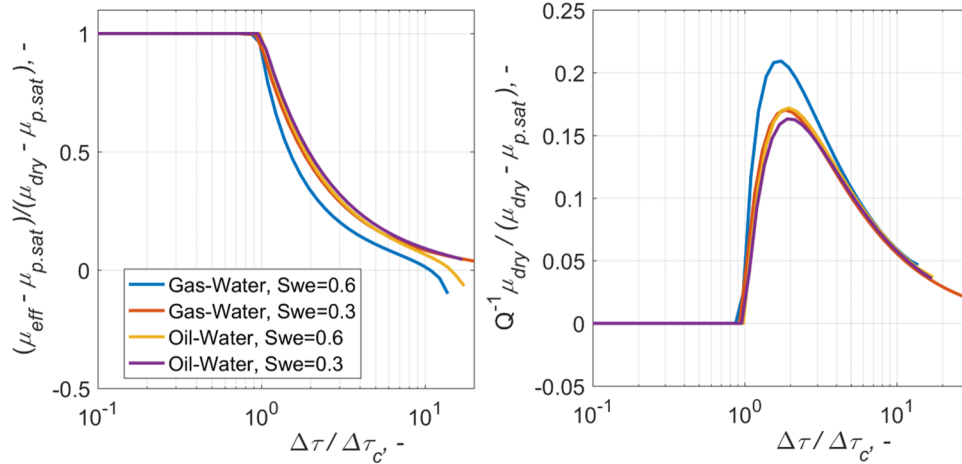


Figure 9 show collapse of data curves of Fig. 8 after scaling of vertical and horizontal axes (all curves follow the same trend). See text for details.

In this form, all input parameters of equation (60) have quite clear physical interpretation. Equation (60) shows no dependence on the fluid bulk moduli. Also, the critical stress amplitude ( $\Delta\tau_c$ ) neither depends on the fluid bulk moduli, according to equation (54). Thus, the shear softening effect does not depend on the fluid bulk moduli. We discussed previously after equation (21) that the current model is applicable both for drained and undrained boundary conditions for both fluids, where the drained boundary conditions can be set by using zero values for fluid bulk moduli. Because equations (54), (55), (60) does not depend on the fluid bulk moduli, it implies that the shear softening does not depend on the fluid boundary conditions during pure shear stress-perturbation experiments, that is the same shear softening effect will be observed for drained and undrained boundary conditions. Let us now apply equations (54) and (55) to explain the diversity of experimental data, shown in Figure 8. We will modify the vertical and horizontal axis of Fig. 8 to demonstrate the ‘data collapse’. The horizontal axis of Fig. 8(a,b) will be scaled by the critical wave amplitude, calculated with equation (54), that is  $\Delta\tau \rightarrow \frac{\Delta\tau}{\Delta\tau_c}$ . The vertical axis of Fig. 8(a) will be scaled by  $\mu_{\text{eff}} \rightarrow \frac{\mu_{\text{eff}} - \mu_{p.\text{sat}}}{\mu_{\text{dry}} - \mu_{p.\text{sat}}}$ , whereas the vertical axis of Fig. 8(b) will be scaled by  $Q^{-1} \rightarrow Q^{-1} \frac{\mu_{\text{dry}}}{\mu_{\text{dry}} - \mu_{p.\text{sat}}}$ . Figure 9 shows calculated results, shown in Fig. 8 after scaling of vertical and horizontal axes. Figure 9 shows the ‘data collapse’ when all curves follows the same trend. The data collapse curves do not coincide exactly because the non-linear effects and iterations are neglected during derivation of equations (54) and (55). However, these equations capture the most important physics and neglect input parameters, which are not important (i.e. bulk

moduli of pore fluids). Equations (55) and (60) show that the shear softening effect is strong in rock with compliant pores in which the capillary pressure is highly sensitive to the change of the confining stress, while if the rock material does not contain compliant pores or cracks the partial derivative,  $\frac{\partial p_{\text{cap}}}{\partial \sigma}$  will be small in this rock, and thus the shear softening effect will be small as well.

## APPLICATION OF THE MODEL TO RESERVOIR ROCKS

In this section, we discuss application of the model to reservoir rocks. The reservoir rocks may contain many cracks of different length and aspect ratio (e.g., Zimmerman 1990; Anders, Laubach and Scholz 2014). Hooker *et al.* (2009) found that the aperture distribution of cracks between grains is best described by log-normal distribution, suggesting that a lower cut-off is attributed to the grain scale. Pruess and Tsang (1990) argued that for the log-normal aperture distribution, a simple approximation to capillary pressure of microcrack (or fracture) system is obtained in closed form that resemble the typical shape of Leverett’s J-function, which is described in reservoir engineering as follows (e.g. Barenblatt *et al.* 1990):

$$p_{\text{cap}} = \frac{\gamma \cos(\theta)}{\sqrt{\kappa_c/n_c}} J(S_{we}), \quad (61)$$

where  $J(S_{we})$  is the dimensionless Leverett’s J-function and  $\kappa_c$  is the permeability of microcrack system and  $n_c$  is the porosity of microcrack system. The Leverett’s J-function is a generalized approach, valid for capillary pressure description both

in consolidated and unconsolidated rocks and for description of capillary pressure in fractures and micro-cracks systems. It must be noted that we are focusing only on microcrack porosity and microcrack permeability in a dual-porosity and dual-permeability rocks. Such differentiation of pore system on compliant pores (cracks or fractures) and stiff pores (matrix) is quite common both in geophysics and reservoir engineering (e.g. Pride and Berryman 2003; Gerke and van Genuchten 1993).

There Leverett J-function can be approximated in its simplest form by the power-law function (Brooks and Corey 1966):

$$J(S_{we}) = s_0 S_{we}^{-\frac{1}{\lambda}}, \quad (62)$$

where  $\lambda > 0$  and  $s_0 > 0$  are empirical dimensionless coefficients,  $\lambda$  is the crack aperture distribution index and  $s_0$  is related to the crack capillary entry pressure, as follows:

$$p_{entry} = \frac{\gamma \cos(\theta)}{\sqrt{\kappa_c/n_c}} s_0. \quad (63)$$

Here for simplicity we consider the following relationships between permeability and porosity of the crack system:

$$\kappa_c = \kappa_0 n_c^3. \quad (64)$$

This relationship follows from the assumption that the crack permeability is proportional to the cube of crack aperture, whereas the crack porosity is linearly proportion to the crack aperture. Due to tortuosity effects, the cubic law scaling relationships between crack porosity and crack permeability may not be always applicable, in this case a different power-law scaling exponent needs to be used, that is  $\kappa_c = \kappa_0 n_c^q$ , with  $q > 3$ .

The porosity (and permeability) of the crack system is highly sensitive to the effective stress, which can be described by crack compressibility (e.g. Zimmerman 1990):

$$\frac{\partial n_c}{\partial \sigma} = n_c C_{pc}, \quad (65)$$

where  $C_{pc}$  is the crack compressibility under constant fluid pressure (e.g. Zimmerman 1990). In the simplest case, if  $C_{pc} = \text{const}$ , equation (65) can be integrated, yielding:  $n_c = n_0 \exp(C_{pc}(\sigma + p_{fl}))$  (e.g. Zimmerman 1990). It must be noted here again that we are using a sign convention when compressive stresses are negative, whereas in engineering and geosciences it is more common to use the sign convention when compressive stresses are positive. Derived equations (54) and (60) (and equation (65)) require that the compressive stress is negative, otherwise these equations must be modified by  $\frac{\partial}{\partial \sigma} \rightarrow -\frac{\partial}{\partial \sigma}$ .

Walsh (1965) derived the following equation for the crack:

$$C_{pc} = \frac{1}{m} \frac{1 - \nu}{\mu_{min}}. \quad (66)$$

Note that according to equation (4), the crack compressibility is reciprocal to crack closure stress, whereas, according to equation (53) it can be related to the crack porosity, dry shear modulus and shear modulus of rock mineral. In equation (66),  $m$  is the aspect ratio of the crack, defined as:

$$m = \frac{W}{L}. \quad (67)$$

Here  $W$  is the crack aperture at given effective stress and  $L$  is the crack length. Experimental data, outlined in Zimmerman (1990, p. 133) shows that the typical values for the aspect ratio distribution function of the sandstone are in the range  $10^{-5} \lesssim m \lesssim 10^{-3}$  with the most frequent value around  $m \sim 10^{-4}$ . Similar range for the crack aspect ratio scaling was suggested for carbonate rocks and granite by (Cheng and Toksöz 1979).

Next, we substitute equations (63)–(66), describing capillary pressure, permeability, porosity and compressibility of microcrack system in natural rocks, to equations (54) and (60), describing the critical wave amplitude ( $\Delta\tau_c$ ) and the shear modulus of partially saturated rock ( $\mu_{p,sat}$ ). After simplification, we derived the following expressions for  $\Delta\tau_c$  and  $\mu_{p,sat}$ :

$$\Delta\tau_c = m \mu_{min} \frac{\theta_a - \theta_r}{1 - \nu} \tan(\theta_Y) \quad (68)$$

and

$$\frac{1}{\mu_{p,sat}} = \frac{1}{\mu_{dry}} + \left( \frac{1}{\mu_{dry}} - \frac{1}{\mu_{min}} \right) \frac{\gamma \cos(\theta_Y)}{\sqrt{\kappa_c/n_c}} \frac{(1 - \nu) \lambda s_0}{\mu_{min} m} S_{we}^{-\frac{1}{\lambda}}, \quad (69)$$

where the Young's angle ( $\theta_Y$ ) is calculated using equation (1), which is approximately equal to  $\theta_Y \approx \frac{\theta_a + \theta_r}{2}$ . The contact angles and interfacial tension can be measured from standard laboratory tests, whereas it extremely difficult to measure other input parameters, such as crack aspect ratio, crack porosity, crack permeability and crack aperture distribution. It is a general problem of any dual-porosity and dual-permeability models, as it is extremely difficult to constrain these input parameters, while at the same time these models can provide physical insights when single-porosity and single-permeability models are not able to.

Next, we consider saturation limits in equation (69). At zero saturation limit ( $S_{we} \rightarrow 0$ ), we have as expected  $\mu_{p,sat} \rightarrow \mu_{dry}$  if  $\lambda > 1$  and  $\mu_{p,sat} \rightarrow 0$  if  $\lambda < 1$ . In granular

material, the typical values for the pore size distribution index  $\lambda$  are in the range  $1 < \lambda < 4.2$  (Brooks and Corey 1966; Laliberte, Corey and Brooks 2007), that is all reported values for  $\lambda$  index are higher than 1. However, those reported values include both pore systems: matrix and cracks, thus one may argue that obtained bounds for  $\lambda$  may not be representative for cracks. It is not difficult to demonstrate that there is a theoretical reason for  $\lambda > 1$ . The value  $\lambda < 1$  would imply that the crack porosity is dominated by cracks with smallest possible aperture that is not possible for consolidated rocks, because it requires infinitely large crack area if the crack porosity is finite. In opposite, values  $\lambda > 1$  imply that the crack porosity is dominated by cracks with highest possible aperture, that is more representative for consolidated rocks. Thus, in the limit  $S_{we} \rightarrow 0$ , equation (69) predicts the expected result:  $\mu_{p.sat} \rightarrow \mu_{dry}$ . The case of full saturation must be discussed with more details. When  $S_{we} \rightarrow 1$ , equation (69) predicts  $\mu_{p.sat} < \mu_{dry}$ ; however, in the case of full saturation, we would also expect  $\mu_{p.sat} = \mu_{dry}$ , according to discussions around Fig. 1(a). Indeed, in the case of full saturation, the capillary pressure is 0 and after substitution of  $p_{cap} = 0$  into equation (60), we will get the expected result  $\mu_{p.sat} = \mu_{dry}$  when  $S_{we} = 1$ . The reason why equation (69) predicts  $\mu_{p.sat} < \mu_{dry}$  when  $S_{we} = 1$  is due to Brooks and Corey (1966) approximation for the capillary pressure. Due to this approximation, the capillary pressure is not 0 in the case of full saturation, according to equation (62). The capillary pressure of rocks drops rapidly to 0 when  $S_{we} \rightarrow 1$ . Thus, Brooks and Corey (1966) approximation is not applicable to explain this end-tail behaviour of the capillary pressure at  $S_{we} \rightarrow 1$ . Thus, according to equation (60), we would expect  $\mu_{p.sat} \rightarrow \mu_{dry}$  in the same manner as  $p_{cap} \rightarrow 0$ , when  $S_{we} \rightarrow 1$ . Thus, if the rock is literally 100% saturated with a single fluid phase, there would not be any liquid bridges and thus no shear softening effect, according to our model. Several authors, who reported the shear softening effect for saturated rocks argued that it was extremely difficult to achieve full saturation of rock sample, especially if the rock sample is tight (e.g. Murphy 1984; Verwer *et al.* 2010; Li *et al.* 2017). Even after applying different advanced saturation techniques, there might be some pores that are not completely saturated, containing entrapped oil or gas bubbles. For example, Li *et al.* (2017) argued that the maximum wetting-phase saturation which was possible to achieve during experiments was around 98%, thus Brooks and Corey approximation is relevant for this case. Furthermore, published literature outlined in Introduction showed that the shear softening effect was not observed on all tested samples of the same rock. There might be several explanations

for why some samples do not reveal the shear softening behaviour. One of the possible explanations is that those samples were fully (100%) saturated, thus capillary pressure in those samples were 0. At the reservoir conditions, when the fluid pressure is above bubble point, we do not expect to have any free gas in the formation. However, in the oil reservoir, we still have the interface menisci between oil and water which reduce the shear modulus. Thus, pore-scale interface phenomena effects are relevant both at the laboratory conditions and at the reservoir conditions.

## DISCUSSIONS

In this section, we would like to discuss the important application of this theory: effect of pore fluids and saturation on mechanical strength. According to linear elastic fracture mechanics, the mechanical stiffness (shear modulus) and strength (tensile or uniaxial compressional) are interrelated properties (e.g. Paterson and Wong 2005). The tensile rock strength and uniaxial compression strength are linearly proportional to the fracture toughness ( $K_{Ic}$ ), whereas the fracture toughness is related to the shear modulus ( $\mu$ ), Poisson's ratio and specific fracture energy ( $G_c$ ) required to brake molecular bonds during propagation of fracture, as follows:

$$K_{Ic} = \sqrt{\mu \frac{2G_c}{1-\nu}}. \quad (70)$$

Thus, the change of shear modulus by pore fluids will affect the mechanical strength of rocks. In equation (70), we consider specific fracture energy ( $G_c$ ) as an intrinsic material property, independent on the fluid content. However, there are some publications where authors assume the change of apparent fracture energy  $G_c$  by pore fluids to explain the water weakening effect (e.g. Bergsaker *et al.* 2016). In this paper, we assume that  $G_c$  is independent on the fluid content, while the weakening is due to apparent change of the shear modulus. Furthermore, because bulk modulus is highly sensitive to pore fluids (Rozhko 2019), the Poisson's ratio in equation (70) is also affected by pore fluids. However, the fracture toughness in equation (70) is much more sensitive to the change of shear modulus, compared to Poisson's ratio, thus at the first-order approximation we can assume  $\nu$  and  $G_c$  to be independent on fluids in equation (70). Thus, using equations (69) and (70), we can estimate the 'fluid weakening' effect as

$$\frac{K_{Ic,p.sat}}{K_{Ic,dry}} = \left( 1 + \left( 1 - \frac{\mu_{dry}}{\mu_{min}} \right) \frac{\gamma \cos(\theta_Y)}{\sqrt{\kappa_c/n_c}} \frac{(1-\nu)}{\mu_{min}} \frac{\lambda s_0}{m} S_{we}^{1-\frac{1}{\lambda}} \right)^{-\frac{1}{2}}, \quad (71)$$

where the ‘weakening’ is referred to the change of strength, whereas ‘softening’ to the change of stiffness.

Equations (69) and (71) predict the decrease of shear modulus and mechanical strength with:

1. increase of the wetting phase saturation;
2. increase of the wettability towards wetting phase (i.e. decrease of  $\theta_Y$ );
3. increase of surface tension between the wetting and non-wetting phases;
4. increase of crack compressibility and crack aperture distribution index.

Next, let us discuss published experimental data, supporting conclusions (1)–(4) of our model. Vutukuri (1974) was one of the first who experimentally demonstrated that the tensile strength of limestone, saturated with different liquids, depends on the liquid/vapor (air) surface tension of pore liquid. His results show that with increasing surface tension in the liquid the tensile strength of the limestone decreases. Similar conclusions about the role of surface tension of pore liquid can be drawn from experimental work of Risnes *et al.* (2003), who demonstrated that oil saturated rock sample (such as chalk) can be significantly stronger than water saturated rock sample and substantially weaker than dry sample. Same observations were systematically recorded for poorly consolidated, weakly cemented sandstones (Rhett and Lord 2001; David *et al.* 2015). The surface tension between water and air interface is larger than surface tension of oil and air interface, whereas there is no (zero) surface tension for dry sample, therefore, the experimental results of Risnes *et al.* (2003) show the same trend: the reduction of mechanical strength with increase of liquid/vapor surface tension. Similar trend follows from experimental work of Risnes *et al.* (2005), who studied the effect of water–glycol mixture on mechanical strength of outcrop chalk. Risnes *et al.* (2005) demonstrated that the mechanical strength of chalk decreased with increased water concentration in water–glycol mixture. Water and ethylene–glycol are fully miscible liquids at atmospheric conditions, and the liquid–vapor surface tension of water/ethylene–glycol mixture increases with water concentration. Thus, experimental work of Risnes *et al.* (2005) is consistent with Vutukuri’s (1974) conclusions. Furthermore, Risnes and Flaageng (1999) and Hedegaard and Graue (2011) pointed out that wettability is an important parameter in the fluid–rock interaction and demonstrated that water flooding of oil-wet (hydrophobic) oil-saturated chalk samples shows strengthening effect, whereas water flooding of water-wet (hydrophilic) oil saturated samples shows the weakening effect. Because wettability and contact angle are inter-related properties, the experimen-

tal work of Risnes and Flaageng (1999) and Hedegaard and Graue (2011) indicates the capillary nature of water weakening phenomenon of carbonates. There are many explanations for the water-weakening effect are suggested in literature: effect of water activity/salinity/pH and so on (Risnes *et al.* 2003; Rostom *et al.* 2013). These explanations are interrelated to each other, because water activity, salinity and pH affect surface tension and contact angles. For example, the addition of inorganic salts to water raises the surface tension approximately linearly with the salt concentration above 0.01 mole/l, whereas at dilute salt concentrations the interfacial tension decreases with salt concentration due to Jones–Ray effect (Petersen and Saykally 2006). Aslan, Fathi Najafabadi and Firoozabadi (2016) show a non-monotonic dependence of the contact angle on smooth surfaces of different rocks as a function of salt concentration. There is a decrease of the contact angle as the NaCl concentration increases and then an increase of the contact angle with a further increase in NaCl concentration. The trend is the same on quartz, mica, and calcite surfaces (Aslan *et al.* 2016). This implies that different salts and salt concentrations alter the capillary properties of pore liquids including surface tension and contact angles.

Several authors argued that the shear softening is lower at higher confining stress (Adam *et al.* 2009; Li *et al.* 2017) due to closure of microcracks. This is also consistent with our theory because crack compressibility is decreasing with increase of confining stress (e.g., Zimmerman 1990). Adam *et al.* (2009) observed decrease of shear modulus with increase of brine saturation at seismic frequency of 100 Hz that is also consistent with our predictions. Vo-Thanh (1995) conducted laboratory measurements of acoustic velocities of sandstone and limestone, saturated with different pore liquids at the different degree of saturation, however we cannot use Vo-Thanh (1995) results for validation of our theory because laboratory measurements were conducted at ultrasonic frequency of 1MHz. The same comment is applied to the recent publication of Bemer, Hamon and Adelinet (2019), who studied dynamic properties of carbonate rock at ultrasonic frequency of 0.5 MHz. They found that unrelaxed shear modulus of the rock saturated with different pore liquids depends on the bulk moduli of pore liquids. It is an expected result as discussed previously around Fig. 1(a). At ultrasonic frequencies, the shear strengthening (due to unrelaxed response) is compensated by shear weakening (due to pore-scale interface phenomena), thus it is not correct to compare ultrasonic measurements neither with Gassmann’s theory nor with the model presented in this paper, because those theories are applicable only for low (seismic) frequencies, below 200 Hz. Mikhaltsevitch *et al.*

**Table 2** Liquid/air surface tensions of pore liquids and sessile drop contact angles on calcite

Liquid	$\gamma$ , (mPa·m)	$\theta_Y$ (Okayama <i>et al.</i> 1997)	$\theta_Y$ (Ethington 1990)
Water	72.8	0°	40° ± 8°
Ethylene Glycol	48	48° ± 2.8°	72° ± 5°
Methanol	23	no data	0°

(2016) conducted dynamic shear modulus measurements at seismic frequencies on carbonate samples, saturated with water, *n*-decane and dry samples. They found that shear modulus of water-saturated samples was about 7% lower than shear modulus of dry samples, whereas the shear modulus of *n*-decane saturated samples was about the same as shear modulus of dry samples. The surface tension for water–air interface is about three times higher than surface tension for *n*-decane–air interface, whereas the contact angles (wettability) were not reported in experiments of Mikhaltsevitch *et al.* (2016), thus it is not possible to compare laboratory results with our model. Contact angles depends on mineralogical composition of rock samples, saturation history, pressure, temperature, roughness of the surface and measurement method, whereas the interface tension between immiscible fluids is the well-defined property, depending only on pressure and temperature. Thus, we cannot use contact angles from external publications to explain results of Mikhaltsevitch *et al.* (2016). Table 2 shows published data by different authors for contact angles of water/air, ethylene-glycol/air and methanol/air interfaces on the calcite (Okayama, Keller and Luner 1997; Ethington 1990). Reported contact angles are quite different for the same substrate mineral and the same fluids. It will of course affect predictions by our model significantly.

Let us consider the example of input parameters, given in Table 3. Those parameters are typical for chalk and taken from different publications given in Table 3. We assumed that the crack aspect ratio, reported for the limestone and dolomite by Cheng and Toksöz (1979) is also representative for chalk. The mercury injection capillary entry pressure into cracks was assumed to be similar to entry pressure, measured on chalk sample reported by Fabricius (2007), whereas the crack aperture distribution index for microcracks in chalk was assumed to be similar to the pore size distribution index for chalk, reported by Christoffersen and Whitson (1995). Figure 10 shows (a) calculated shear modulus, (b) fracture toughness and (c) capillary pressure of chalk, partially saturated with different liquid and gas system. As it was discussed in the pre-

**Table 3** Input parameters for chalk

Property	Value	Reference
Shear modulus of calcite ( $\mu_{\min}$ )	32 GPa	Mavko <i>et al.</i> (2009)
Poisson's ratio of calcite ( $\nu_{\min}$ )	0.32	Mavko <i>et al.</i> (2009)
Shear modulus of dry chalk ( $\mu_{\text{dry}}$ )	8 GPa	Fabricius (2007)
Mercury injection capillary entry pressure for chalk ( $p_{\text{entry,Hg}}$ )	2.1 MPa	Fabricius (2007)
Crack aspect ratio	$0.5 \times 10^{-4}$	Cheng and Toksöz (1979)
Crack aperture distribution index ( $\lambda$ )	3.4	Christoffersen and Whitson (1995)

vious section, due to Brooks and Corey (1966) approximation, the capillary pressure is not vanishing to zero at full saturation. Thus, after substitution of  $p_{\text{cap}} = 0$  into equation (60), we will get the expected results  $\mu_{p,\text{sat}} = \mu_{\text{dry}}$  and  $K_{Ic,p,\text{sat}} = K_{Ic,\text{dry}}$ . Figure 10(a,b) shows that shear modulus and fracture toughness are highly sensitive both to saturation, surface tension and contact angle measurement. The reduction of compressive strength by the degree of water saturation is a well-known effect in rock mechanics (Papamichos, Brignoli and Santarelli 1997; Fjær *et al.* 2008). Figure 10(b) can be compared with experimental data for compressive strength of chalk, reported by Risnes *et al.* (2005), who demonstrated that methanol-saturated chalk sample is stronger than water-saturated chalk sample, but weaker than Ethylene–Glycol saturated chalk sample, while dry rock sample were the strongest. Dashed curves of Fig. 10(b) show the same trend, where the dashed curves are based on contact angle measurements of corresponding liquids on calcite samples from Mexico (Ethington 1990). Using equation (68), we can also estimate the critical wave amplitude when the shear softening is expected. Thus, for the water saturated sample and the contact angle, reported by Okayama *et al.* (1997), we have  $\Delta\tau_c = 0$ . This result indicates that for the complete wetting surface the slippage condition (and shear softening) will not depend on the wave amplitude. Results would be quite different if we would use contact angles reported by Ethington (1990). Ethington (1990) reported averaged advancing and receding contact angles for water air interface on calcite as  $\theta_a \approx 47^\circ$  and  $\theta_r \approx 7^\circ$ , those angles are quite different from Sessile drop contact angle  $\theta_Y \approx 72^\circ$ , while the reason for this difference was not discussed by Ethington (1990). Thus, if we would use advancing and receding angles in equations (1) and (68) we will get  $\Delta\tau_c = 0.852$  MPa. The stress amplitude of 0.852 MPa is

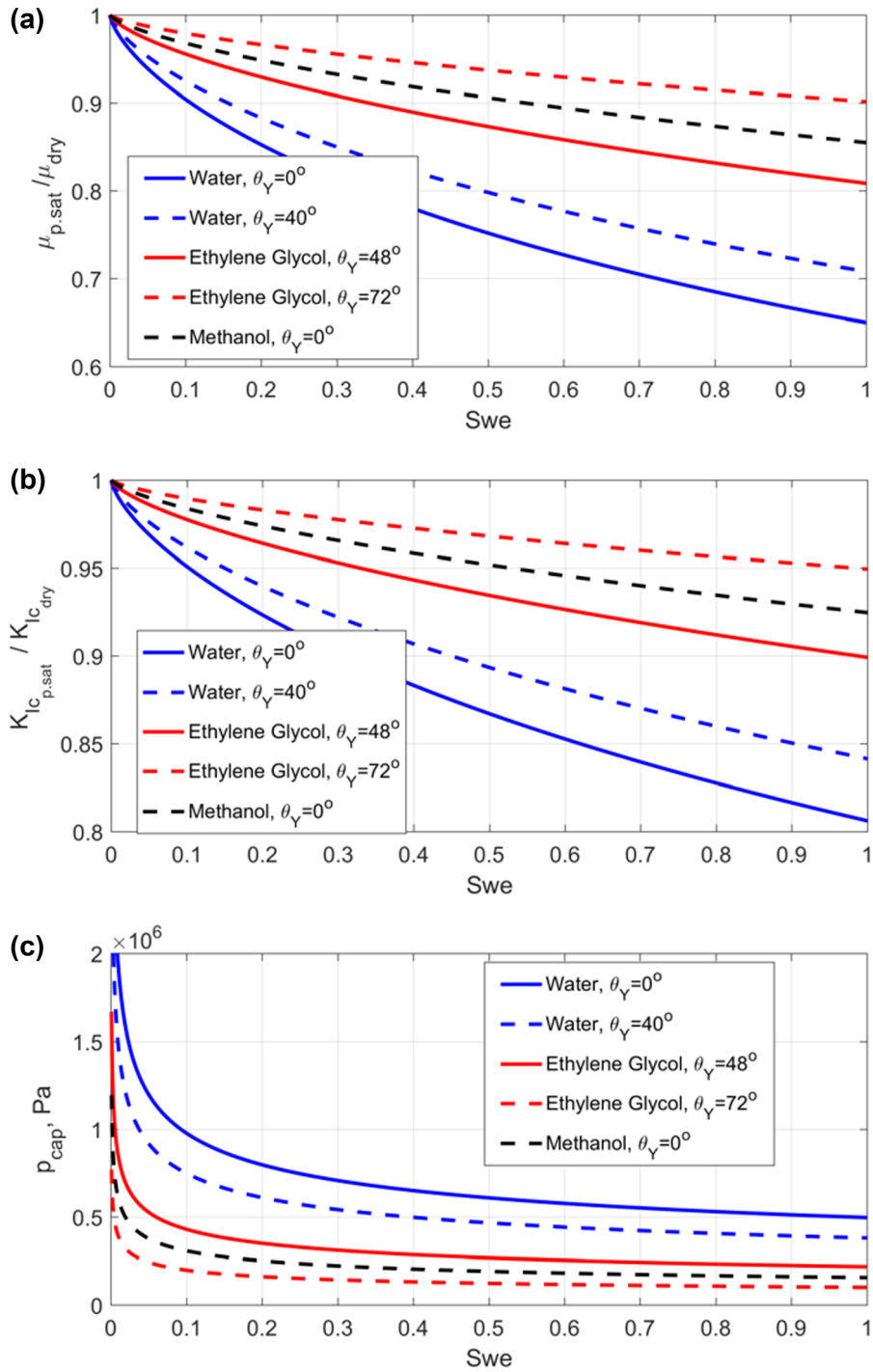


**Figure 10** Effect of pore liquids (water, ethylene glycol and methanol) and saturation on (a) shear modulus; (b) fracture toughness and (c) capillary pressure of chalk (calculated results). Horizontal axis in (a), (b) and (c) shows liquid saturation of microcracks in liquid–air system. Continuous and dashed curves correspond to contact angles measurements on calcite by Okayama *et al.* (1997) and Ethington (1990), respectively. See Tables 2 and 3 for input parameters.

much larger than stress amplitude typical for seismic waves ( $10^2 - 10^4$  Pa). Thus, the shear softening at seismic wave amplitudes may not always be observed, as it is highly sensitive towards wettability of the rock.

## CONCLUSIONS


- The current paper suggests explanation to the effect of pore fluid on quasi-static shear modulus of isotropic partially saturated rock. It is demonstrated that the shear softening is related to the pore-scale interfacial phenomena effects, specifically, to the slippage and rolling of fluid molecules over the surface of the solid at the contact line location during the contact line motion. Classical Biot–Gassmann's models assume Stoke's no-slip boundary conditions between fluid and solid, while due to slippage at the solid–fluid interface the shear modulus of partially saturated rock can be lower than shear modulus of dry rocks. The slippage condition depends not only on material and fluid properties, but also on the wave amplitude. Only for the complete wetting surface, the slippage condition will not depend on the wave amplitude. It is demonstrated that the quasi-static shear modulus of partially saturated rock is sensitive to the following fluid properties: interfacial tension between immiscible fluids, fluid saturation and rock wettability (contact angles) towards saturating fluids and independent on bulk moduli of pore fluids.
- Developed closed form equation allowing to estimate the shear modulus of a partially saturated rock and considering the following additional parameters: capillary pressure, stress sensitivity of capillary pressure and saturation sensitivity of capillary pressure. The shear softening is demonstrated to be possible only in rocks with dual porosity and dual permeability. Also, we predicted the critical wave amplitude defining the onset of shear softening. If the wave amplitude is lower than the critical amplitude, the shear modulus of partially saturated rock will be equal to shear modulus of dry rock, whereas if the wave amplitude is higher than its critical value, then the shear softening effect will take place. This derived equation depends on advancing and receding contact angles, wettability sensitivity of capillary pressure and stress sensitivity of capillary pressure.
- Suggested model was applied to estimate the shear softening and shear weakening effects of pore fluids in natural rocks with log-normal distribution of micro-crack aperture. In such rocks, the capillary pressure of microcrack system was described by Leverett's J-function with Brook–Corey's

saturation dependency. Derived closed-form analytical solutions explain alteration of shear modulus and strength by pore fluids and saturation.

## ACKNOWLEDGEMENTS

I would like to thank Mahyar Madadi and anonymous reviewer for comments and suggestions improving the manuscript.

## ORCID

Alexander Y. Rozhko   
<https://orcid.org/0000-0002-3866-8714>

## REFERENCES

- Adam L., Batzle M. and Brevik, I. 2006. Gassmann's fluid substitution and shear modulus variability in carbonates at laboratory seismic and ultrasonic frequencies. *Geophysics* **71**, F173–F183.
- Adam L., Batzle M., Lewallen K.T. and van Wijk K. 2009. Seismic wave attenuation in carbonates. *Journal of Geophysical Research: Solid Earth* **114**.
- Adam L. and Ortheim T. 2013. Elastic laboratory measurements and modeling of saturated basalts. *Journal of Geophysical Research: Solid Earth* **118**, 840–851.
- Anders M.H., Laubach S.E. and Scholz C.H. 2014. Microfractures: a review. *Journal of Structural Geology* **69**, 377–394.
- Aslan S., Fathi Najafabadi N. and Firoozabadi A. 2016. Non-monotonicity of the contact angle from NaCl and MgCl<sub>2</sub> concentrations in two petroleum fluids on atomistically smooth surfaces. *Energy & Fuels* **30**, 2858–2864.
- Assefa S., McCann C. and Sothcott J. 2003. Velocities of compressional and shear waves in limestones. *Geophysical Prospecting* **51**, 1–13.
- Baechele G.T., Eberli G.P., Weger R.J. and Massaferro J.L. 2009. Changes in dynamic shear moduli of carbonate rocks with fluid substitution. *Geophysics* **74**, E135–E147.
- Baechele G.T., Weger R.J., Eberli G.P., Massaferro J.L. and Sun Y.F. 2005. Changes of shear moduli in carbonate rocks: implications for Gassmann applicability. *The Leading Edge* **24**, 507–510.
- Barenblatt G.I., Entov V.M. and Ryzhik V.M. 1990. *Theory of Fluid Flows Through Natural Rocks*. Kluwer Academic Publishers.
- Baud P., Zhu W. and Wong T.F. 2000. Failure mode and weakening effect of water on sandstone. *Journal of Geophysical Research: Solid Earth* **105**, 16371–16389.
- Bauer A., Bhuiyan M.H., Fjær E., Holt R.M., Lozovyi S., Pohl M. et al. 2016. Frequency-dependent wave velocities in sediments and sedimentary rocks: laboratory measurements and evidences. *The Leading Edge* **35**, 490–494.
- Bemer E., Hamon Y. and Adelinet M. 2019. Consistent experimental investigation of the applicability of Biot-Gassmann's equation in carbonates. *Geophysics* **84**, 1–92.



- Bergsaker A.S., Røyne A., Ougier-Simonin A., Aubry J. and Renard F. 2016. The effect of fluid composition, salinity, and acidity on subcritical crack growth in calcite crystals. *Journal of Geophysical Research: Solid Earth* **121**, 1631–1651.
- Berryman J.G. 2005. Pore fluid effects on shear modulus in a model of heterogeneous rocks, reservoirs, and granular media. *Journal of Geophysical Research: Solid Earth* **110**.
- Bhuiyan M.H. and Holt R.M. 2016. Variation of shear and compressional wave modulus upon saturation for pure pre-compacted sands. *Geophysical Journal International* **206**, 487–500.
- Bormashenko E.Y. 2013a. *Wetting of Real Surfaces*, Vol. 19. Walter de Gruyter.
- Bormashenko E. 2013b. Wetting of real solid surfaces: new glance on well-known problems. *Colloid and Polymer Science* **291**, 339–342.
- Brooks R.H. and Corey A.T. 1966. Properties of porous media affecting fluid flow. *Journal of the Irrigation and Drainage Division* **92**, 61–90.
- Chen H., Amirfazli A. and Tang T. 2013. Modeling liquid bridge between surfaces with contact angle hysteresis. *Langmuir* **29**, 3310–3319.
- Cheng C.H. and Toksöz M.N. 1979. Inversion of seismic velocities for the pore aspect ratio spectrum of a rock. *Journal of Geophysical Research: Solid Earth* **84**, 7533–7543.
- Chibowski E. 2008. Surface free energy of sulfur—Revisited I. Yellow and orange samples solidified against glass surface. *Journal of Colloid and Interface Science* **319**, 505–513.
- Christoffersen K.R. and Whitson C.H. 1995. Gas/oil capillary pressure of chalk at elevated pressures. *SPE Formation Evaluation* **10**, 153–159.
- David C., Dautriat J., Sarout J., Delle Piane C., Menéndez B., Macault R. *et al.* 2015. Mechanical instability induced by water weakening in laboratory fluid injection tests. *Journal of Geophysical Research: Solid Earth* **120**, 4171–4188.
- De Gennes P.G., Brochard-Wyart F. and Quéré D. 2013. *Capillarity and Wetting Phenomena: Drops, Bubbles, Pearls, Waves*. Springer Science & Business Media.
- De Souza E.J., Gao L., McCarthy T.J., Arzt E. and Crosby A.J. 2008. Effect of contact angle hysteresis on the measurement of capillary forces. *Langmuir* **24**, 1391–1396.
- Diethart-Jauk E. and Gegenhuber N. 2018. Shear weakening for different lithologies observed at different saturation stages. *Journal of Applied Geophysics* **148**, 107–114.
- Ethington E.F. 1990. *Interfacial contact angle measurements of water, mercury, and 20 organic liquids on quartz, calcite, biotite, and Ca-montmorillonite substrates (Report No. 90–409)*. US Geological Survey.
- Fabricius I.L. 2007. Chalk: composition, diagenesis and physical properties. *Bulletin of the Geological Society of Denmark* **55**, 97–128.
- Fabricius I.L., Bächle G.T. and Eberli G.P. 2010. Elastic moduli of dry and water-saturated carbonates—Effect of depositional texture, porosity, and permeability. *Geophysics* **75**, N65–N78.
- Fjær E., Holt R.M., Raaen A.M., Risnes R. and Horsrud P. 2008. *Petroleum Related Rock Mechanics*, Vol. 53. Elsevier.
- Gassmann F. 1951. Über die Elastizität poröser Medien. *Vierteljahrsschrift der Naturforschenden Gesellschaft in Zürich* **96**, 1–23.
- Gegenhuber N. 2015. Application of Gassmann's equation for laboratory data from carbonates from Austria. *Austrian Journal of Earth Sciences* **108**, 239–244.
- Gerke H.H. and Genuchten M.V. 1993. A dual-porosity model for simulating the preferential movement of water and solutes in structured porous media. *Water Resources Research* **29**, 305–319.
- Hedegaard K. and Graue, A. 2011. Does wettability affect the strength of chalk? *45th U.S. Rock Mechanics/Geomechanics Symposium, June, San Francisco, California*. American Rock Mechanics Association.
- Hooker J.N., Gale J.F.W., Gomez L.A., Laubach S.E., Marrett R. and Reed R.M. 2009. Aperture-size scaling variations in a low-strain opening-mode fracture set, Cozzette Sandstone, Colorado. *Journal of Structural Geology* **31**, 707–718.
- Japsen P., Høier C., Rasmussen K.B., Fabricius I., Mavko G. and Pedersen J.M. 2002. Effect of fluid substitution on ultrasonic velocities in chalk plugs, South Arne field, North Sea. *SEG Technical Program, Expanded Abstracts*, 1881–1884.
- Khazanehdari J. and Sothcott J. 2003. Variation in dynamic elastic shear modulus of sandstone upon fluid saturation and substitution. *Geophysics* **68**, 472–481.
- Laliberte G.E., Corey A.T. and Brooks R.H. 2007. *Properties of unsaturated porous media*. Hydrology papers No. 17. Colorado State University.
- Lebedev M, Wilson M.E. and Mikhaltsevitch V. 2014. An experimental study of solid matrix weakening in water-saturated Savonnières limestone. *Geophysical Prospecting* **62**, 1253–1265.
- Li D., Wei J., Di B., Ding P., Huang S. and Shuai D. 2018. Experimental study and theoretical interpretation of saturation effect on ultrasonic velocity in tight sandstones under different pressure conditions. *Geophysical Journal International* **212**, 2226–2237.
- Li D., Wei J., Di B., Ding P. and Shuai D. 2017. The effect of fluid saturation on the dynamic shear modulus of tight sandstones. *Journal of Geophysics and Engineering* **14**, 1072.
- Mavko G. and Jizba D. 1991. Estimating grain-scale fluid effects on velocity dispersion in rocks. *Geophysics* **56**, 1940–1949.
- Mavko G., Mukerji T. and Dvorkin J. 2009. *The Rock Physics Handbook: Tools for Seismic Analysis of Porous Media*. Cambridge University Press.
- Mavko G., Mukerji T. and Dvorkin J. 2014. *Effective medium models*. Stanford, CA: Stanford University. <https://pangea.stanford.edu/courses/gp262/Notes/9.EffectiveMediumTheories.pdf>
- Mikhaltsevitch V., Lebedev M. and Gurevich B. 2016. Laboratory measurements of the effect of fluid saturation on elastic properties of carbonates at seismic frequencies. *Geophysical Prospecting* **64**, 799–809.
- Murphy W.F. 1984. Acoustic measures of partial gas saturation in tight sandstones. *Journal of Geophysical Research: Solid Earth* **89**, 11549–11559.
- Murphy W.F. III, Winkler K.W. and Kleinberg R.L. 1986. Acoustic relaxation in sedimentary rocks: dependence on grain contacts and fluid saturation. *Geophysics* **51**, 757–766.
- Müller T.M., Gurevich B., and Lebedev M. 2010. Seismic wave attenuation and dispersion resulting from wave-induced flow in porous rocks—A review. *Geophysics* **75**, 75A147–75A164.

- Okayama T., Keller D.S. and Luner P. 1997. The wetting of calcite surfaces. *The Journal of Adhesion* **63**, 231–252.
- Papamichos E., Brignoli M. and Santarelli F.J. 1997. An experimental and theoretical study of a partially saturated collapsible rock. *Mechanics of Cohesive-frictional Materials: An International Journal on Experiments, Modelling and Computation of Materials and Structures* **2**, 251–278.
- Paterson M.S. and Wong T.F. 2005. *Experimental Rock Deformation—the Brittle Field*. Springer Science & Business Media.
- Petersen P.B. and Saykally R.J. 2006. On the nature of ions at the liquid water surface. *Annual Review of Physical Chemistry* **57**, 333–364.
- Pruess K. and Tsang Y.W. 1990. On two-phase relative permeability and capillary pressure of rough-walled rock fractures. *Water Resources Research* **26**, 1915–1926.
- Pride S.R. and Berryman J.G. 2003. Linear dynamics of double-porosity dual-permeability materials. I. Governing equations and acoustic attenuation. *Physical Review E* **68**, 036603.
- Pride S.R., Berryman J.G. and Harris J.M. 2004. Seismic attenuation due to wave-induced flow. *Journal of Geophysical Research: Solid Earth* **109**.
- Ren W. and Weinan E. 2007. Boundary conditions for the moving contact line problem. *Physics of Fluids* **19**, 022101.
- Regnet J.B., Robion P., David C., Fortin J., Brigaud B. and Yven B. 2015. Acoustic and reservoir properties of microporous carbonate rocks: Implication of micrite particle size and morphology. *Journal of Geophysical Research: Solid Earth* **120**, 790–811.
- Rhett D.W. and Lord C.J. (2001). Water weakening in sedimentary rocks. *DC Rocks 2001, the 38th US Symposium on Rock Mechanics (USRMS)*. American Rock Mechanics Association.
- Rostom F., Røyne A., Dysthe D.K. and Renard F. 2013. Effect of fluid salinity on subcritical crack propagation in calcite. *Tectonophysics* **583**, 68–75.
- Rozhko A.Y. 2016. Two-phase fluid-flow modeling in a dilatant crack-like pathway. *Journal of Petroleum Science and Engineering* **146**, 1158–1172.
- Rozhko A.Y. 2019. Bulk moduli and seismic attenuation in partially saturated rocks: hysteresis of liquid bridges effect. *Geophysical Prospecting* **67**, 1404–1430.
- Rozhko A.Y. and Bauer A. 2018. Contact line friction and surface tension effects on seismic attenuation and effective bulk moduli in rock with a partially-saturated crack. *Geophysical Prospecting* **67**, 913–934.
- Risnes R. and Flaageng O. 1999. Mechanical properties of chalk with emphasis on chalk-fluid interactions and micromechanical aspects. *Oil & Gas Science and Technology* **54**, 751–758.
- Risnes R., Haghghi H., Korsnes R.I. and Natvik O. 2003. Chalk-fluid interactions with glycol and brines. *Tectonophysics* **370**, 213–226.
- Risnes R., Madland M.V., Hole M. and Kwabiah N.K. 2005. Water weakening of chalk—Mechanical effects of water-glycol mixtures. *Journal of Petroleum Science and Engineering* **48**, 21–36.
- Røgen B., Fabricius I.L., Japsen P., Hoier C., Mavko G. and Pedersen J.M. 2005. Ultrasonic velocities of North Sea chalk samples: influence of porosity, fluid content and texture. *Geophysical Prospecting* **53**, 481–496.
- Ruiz-Cabello F.M., Rodríguez-Valverde M.A. and Cabrerizo-Vilchez M.A. 2014. Equilibrium contact angle or the most-stable contact angle? *Advances in Colloid and Interface Science* **206**, 320–327.
- Santos J.E., Douglas, J. Jr, Corberó J. and Lovera O.M. 1990. A model for wave propagation in a porous medium saturated by a two-phase fluid. *The Journal of the Acoustical Society of America* **87**, 1439–1448.
- Schmeling H. 1985. Numerical models on the influence of partial melt on elastic, anelastic and electric properties of rocks. Part I: elasticity and anelasticity. *Physics of the Earth and Planetary Interiors* **41**, 34–57.
- Sharma R., Prasad M., Batzle M. and Vega S. 2013. Sensitivity of flow and elastic properties to fabric heterogeneity in carbonates. *Geophysical Prospecting* **61**, 270–286.
- Shi Z., Zhang Y., Liu M., Hanaor D.A. and Gan Y. 2018. Dynamic contact angle hysteresis in liquid bridges. *Colloids and Surfaces A: Physicochemical and Engineering Aspects* **555**, 365–371.
- Tadmor R. 2004. Line energy and the relation between advancing, receding, and young contact angles. *Langmuir* **20**, 7659–7664.
- Tutuncu A.N., Podio A.L. and Sharma M.M. 1998. Nonlinear viscoelastic behavior of sedimentary rocks, Part II: hysteresis effects and influence of type of fluid on elastic moduli. *Geophysics* **63**, 195–203.
- Vega S., Prajapat J.V. and Al Mazrooei A.A. 2010. Preliminary experiments to evaluate the Gassmann equation in carbonate rocks: Calcite and dolomite. *The Leading Edge* **29**, 906–911.
- Verwer K., Braaksma H. and Kenter J.A. 2008. Acoustic properties of carbonates: effects of rock texture and implications for fluid substitution. *Geophysics* **73**, B51–B65.
- Verwer K., Eberli G., Baechle G. and Weger R. 2010. Effect of carbonate pore structure on dynamic shear moduli. *Geophysics* **75**, E1–E8.
- Vo-Thanh D. 1995. Influence of fluid chemistry on shear-wave attenuation and velocity in sedimentary rocks. *Geophysical Journal International* **121**, 737–749.
- Vutukuri V.S. 1974. The effect of liquids on the tensile strength of limestone. *International Journal of Rock Mechanics and Mining Sciences & Geomechanics Abstracts* **11**, 27–29.
- Walsh J.B. 1965. The effect of cracks on the compressibility of rock. *Journal of Geophysical Research* **70**, 381–389.
- Wang Z., Schmitt D.R. and Wang R. 2015. Does wettability influence seismic wave propagation in liquid-saturated porous rocks? *Geophysical Journal International* **203**, 2182–2188.
- Yaminsky V.V. 2000. Molecular mechanisms of hydrophobic transitions. *Journal of Adhesion Science and Technology* **14**, 187–233.
- Yin H., Borgomano J.V., Wang S., Tiennot M., Fortin J. and Guéguen Y. 2019. Fluid substitution and Shear weakening in clay-bearing sandstone at seismic frequencies. *Journal of Geophysical Research: Solid Earth* **124**, 1254–1272.
- Zhang Y. 2016. *Static and dynamic behaviour of inter-granular liquid bridges: hysteresis of contact angle and capillary forces*. Master's thesis, University of Sydney.
- Zimmerman R.W. 1990. *Compressibility of Sandstones*, Vol. **29**. Elsevier.